

Supplementary Information for

Trajectories for the evolution of bacterial CO₂-concentrating mechanisms

Avi I. Flamholz^{1,2,3,*†}, Eli Dugan^{1,*}, Justin Panich⁴, John J. Desmarais¹, Luke M. Oltrogge¹, Woodward W. Fischer^{3,5}, Steven W. Singer⁴, David F. Savage^{1,6,†}

¹ Department of Molecular and Cell Biology, University of California, Berkeley, California 94720, United States

² Division of Biology and Biological Engineering, California Institute of Technology, Pasadena, CA 91125

³ Resnick Sustainability Institute, California Institute of Technology, Pasadena, CA 91125, USA

⁴ Biological Systems and Engineering Division, Lawrence Berkeley National Laboratory, Berkeley, CA 94720, USA

⁵ Division of Geological & Planetary Sciences, California Institute of Technology, Pasadena, CA 91125

⁶ Howard Hughes Medical Institute, University of California, Berkeley, California 94720

* Equal contribution

† Corresponding Authors: Avi I. Flamholz, David F. Savage

Emails: aflamhol@caltech.edu, savage@berkeley.edu

This PDF file includes:

Supplementary text

Figures S1 to S14

SI References

Other supplementary materials for this manuscript include the following:

Supplementary Tables S1-S5

Supplementary Methods	3
Plasmid Construction	3
Electroporation of CCMB1 <i>E. coli</i>	3
Manipulation of the <i>C. necator</i> genome	3
Plasmid transformation of <i>C. necator</i>	4
Modeling the co-limitation of autotrophic growth	5
Carbonic anhydrase cannot reasonable act as a CO ₂ pump alone	5
A model of autotrophy including the HCO ₃ ⁻ -dependence of growth	6
Choosing realistic ranges for parameter values	8
On the requirement for bicarbonate for biosynthesis	9
Supplementary Figures	11
Supplementary References	25

Supplementary Methods

Plasmid Construction

Genes of interest were amplified by PCR and cloned into their respective vectors using Gibson Assembly. Plasmids were then transformed into chemically competent NEB Turbo *E. coli* cells in most cases. Single colonies were inoculated into 5-8 mL LB media with appropriate antibiotics and mini-prepped once turbid (Qiagen QIAprep spin kit). For the construction of p1Ac, which constitutively expresses *prk*, we used CCMB1 as the cloning strain (1). In addition, to ensure that *prk* expression was not deleterious, as it is for wild-type *E. coli* (2), CCMB1:p1Ac transformants were cultured in a *prk*-dependent manner M9 glycerol media. Plasmid sequences were verified by Sanger sequencing at the UC Berkeley DNA sequencing facility. Details of plasmids used in this study are documented in Table S5 and plasmids have been deposited to Addgene at https://www.addgene.org/David_Savage/.

Electroporation of CCMB1 *E. coli*

Electrocompetent CCMB1 stocks were prepared by standard methods from cultures grown in LB media under 10% CO₂. Plasmids were transformed via electroporation with the following protocol. A 50 µl aliquot of electrocompetent CCMB1 was placed on ice until thawed. 100 ng of mini-prepped plasmid (100 ng each if a double transformation) was then added, gently mixed, and left to incubate for 10 minutes. The transformation aliquot was subsequently transferred to a chilled 1 mm cuvette (Biorad Gene Pulser) and pulsed in a Gene Pulser Xcell Microbial System electroporator (1800 V, 200Ω, 25µF). 500 µl SOC was added to the cuvette and the resulting culture was pipetted into a 14 ml round-bottom falcon tube and placed in 10% CO₂ to incubate for 1 hour. Elevated CO₂ was found to be critical to ensure that CCMB1 recovery is independent of the transformed plasmid(s). After incubation, 200 µl of the culture was plated on an LB agar plate with appropriate antibiotics. When preparing S17 *E. coli* donor cells for conjugation with *C. necator*, plasmids were transformed by the same method, except the recovery was done in ambient CO₂ for 30 minutes.

Spotting assays of CO₂ dependent viability

Figure 1B and Figure S8 report spotting-based titer plating assays of *H. neapolitanus* and CCMB1 *E. coli* strains respectively. For these assays, precultures of the respective strains were grown in liquid media in high CO₂. Stationary phase precultures were diluted to a defined optical density (600 nm, Genesys 20 spectrophotometer, Thermo Scientific) after which they were tenfold serial diluted in media a 96-well plate. 3 µl of tenfold serial dilutions were then spotted on agar plates with appropriate antibiotics. Plates were dried in a laminar flow hood before and after spotting. After the spots dried, plates were incubated in the reported CO₂ conditions in a CO₂ controlled incubator (S41i, New Brunswick). After growth for a defined period of time, colonies were counted in the highest dilution to show > 1 colony and colony forming units (CFU/OD/mL) were back-calculated from the dilution factor, spotted volume and optical density.

Precultures for the *H. neapolitanus* spotting assay reported in Figure 1B were grown in DSMZ-68 media in 5% CO₂ on a platform shaker (New Brunswick Scientific Innova 2000, 200 RPM) in a Percival Intellus Incubator and then washed and diluted to OD 0.1 in DSMZ-68 lacking pH indicator and thiosulfate before spotting. Tenfold dilutions were plated on DSMZ-68 agar plates supplemented with spectinomycin (10

µg/mL) for the mutants but not the wild-type, which lacks a resistance marker. Precultures for the *E. coli* experiment reported in Figure S8 were grown in 10% CO₂ in a CO₂ controlled incubator (S41i, New Brunswick) in M9 glycerol media supplemented with 30 µg/ml kanamycin, 12.5 µg/ml chloramphenicol. *E. coli* strains that cannot grow in minimal medium (e.g. CCMB1 strains lacking rubisco) were precultured in LB media in 10% CO₂. Cultures were then washed and diluted in M9 media with no carbon source (i.e. without glycerol) and spotted onto M9 glycerol plates supplemented with 12.5 µg/ml chloramphenicol. Both *E. coli* and *H. neapolitanus* plates were incubated for 4 days before counting. The relevant strains and plasmids are documented in Tables S4 and S5 respectively.

Manipulation of the *C. necator* genome

The knockout mutant *C. necator* $\Delta A0006 \Delta can \Delta caa$ was produced by iterative rounds homologous recombination (to generate a desired mutation) followed by *sacB* counterselection to cure the kanamycin resistance marker integrated at the target locus (3). Homologous recombination was achieved by conjugation with *E. coli* S17 carrying a mobilizable vector encoding 500 bp homology arms flanking a cassette encoding kanamycin resistance and *sacB* counter selection. For each individual knockout, a pKD19-mobSacB plasmid was generated with 500 bp homology arms directly flanking the target gene. This plasmid was transformed into *C. necator* by conjugation with *E. coli* S17 and plated onto LB agar supplemented with 200 µg/ml kanamycin to select for integrants and 10 µg/ml gentamicin to select against residual *E. coli*.

Single integrant colonies were inoculated into LB with 10 µg/ml gentamicin and 20 µg/ml kanamycin and incubated in 30 °C until turbid. Genomic integration was verified by colony PCR using a primer set where one primer annealed to the genome and the other primer annealed to the plasmid backbone. Verified colonies were inoculated into salt-free LB (10 g/L tryptone, 5 g/L yeast extract) supplemented with 10 µg/ml gentamicin and 100 mg/ml sucrose and incubated at 30 °C for 48-72 hours to select against *sacB* activity. Strains were then streaked on two different LB plates: one without NaCl, but containing 10 µg/ml gentamicin and 50 mg/ml sucrose and a second plate with NaCl, 10 µg/ml gentamicin and 200 µg/ml kanamycin. Colonies that grew on sucrose but not on kanamycin were genotyped by colony PCR using a pair of primers that annealed upstream and downstream of the target gene. PCRs were run on an agarose gel to ensure prospective knockouts were not wild-type revertants. The final strain, *C. necator* $\Delta A0006 \Delta can \Delta caa$ was further verified by phenotype: it fails to grow heterotrophically in ambient air, but is able to grow under elevated CO₂ (4, 5).

Plasmid transformation of *C. necator*

To enable routine electroporation of plasmids into *C. necator* H16, we first knocked out the *hdsR* homolog *A0006* as removal of this restriction enzyme increases electroporation efficiency (3, 6). Electrocompetent stocks of *C. necator* $\Delta A0006$ -derived strains (including the various knockouts) were made according to a protocol from (3) with the following modifications. A colony of the strain was inoculated into LB with 10 µg/ml gentamicin. Once turbid, the pre-culture was added to 100 mL fresh media and let grow until it reached an OD₆₀₀ between 0.6-0.8. $\Delta A0006$ was grown in ambient CO₂ and $\Delta A0006 \Delta can \Delta can$ was grown in 10% CO₂. Cells were then chilled, shaking in an ice slurry until they reached 4 °C. The culture was split into two 50 ml Falcon tubes and centrifuged at 4000g for 10 minutes at 4 °C. The supernatant was decanted and pellets were washed twice with 50 ml ice cold sterile water

and once with 50 ml 10% glycerol. The pellets were then resuspended in 0.75 ml 10% glycerol, pooled, and 100 μ l aliquots were flash-frozen in liquid nitrogen for storage at -80 °C.

For plasmid transformation, a 100 μ l aliquot of *C. necator* was thawed on ice. Upon thawing, 500 ng of plasmid was added, gently mixed, and left to incubate on ice for 5 minutes. The aliquot was then transferred to a 1 mm electroporation cuvette (Biorad Gene Pulser) and pulsed in a Gene Pulser Xcell Microbial System electroporator (2300 V, 200 Ω , 25 μ F). The sample was then immediately resuspended in 1 ml of LB supplemented with 10 mg/ml fructose, transferred into a 14 ml round-bottom falcon tube, and recovered in a 30 °C for 2 hours (H16 $\Delta A0006$ in ambient CO₂, H16 $\Delta A0006\Delta can\Delta caa$ in 10% CO₂). 200 μ l was then plated on LB agar plates with 10 μ g/ml gentamicin, 200 μ g/ml kanamycin, and 10 mg/ml fructose and placed in a 30 °C incubator at ambient CO₂ or 10% CO₂ (depending on the strain) for 48 hours.

Modeling, data and analysis

The dual-limitation model was elaborated in Mathematica 12 (Wolfram) and steady-state solutions were translated to Python for further analysis and plotting. All data analysis was performed using Python 3.8 and Jupyter notebooks. Data and code required to generate all figures is available at https://github.com/flamholz/ccm_evolution.

Modeling the co-limitation of autotrophic growth

Carbonic anhydrase cannot reasonably act as a CO₂ pump alone

Our model considers an autotroph with no CCM that uses rubisco to fix CO₂ in an environment with fixed extracellular CO₂ and HCO₃⁻ concentrations, C_{out} and H_{out}. We further assume that these extracellular species are in equilibrium with respect to the pH, i.e. that H_{out}/C_{out} = K_{EQ}(pH), and that the intracellular pH is the same as the extracellular pH so that the pH-dependent equilibrium constant K_{EQ}(pH) is equal on both sides of the cell membrane. This assumption of equal pH equilibrium is not required but simplifies the model (7). We now write differential equations describing the time evolution of the intracellular CO₂ and HCO₃⁻ concentrations, C_{in} and H_{in}, at first ignoring the HCO₃⁻ dependence of growth to illustrate that it must be included.

Since CO₂ and HCO₃⁻ have diffusion constants of $\approx 10^3 \mu\text{m}^2/\text{s}$ in water, corresponding to diffusion timescales of $R^2/6D \approx 10^{-4} \text{ s}$ over the ≈ 1 micron lengths of bacterial cells, we assume that their concentrations are spatially homogeneous inside and outside the cell (8). While cytoplasm is more viscous than water (9, 10), these effects depend on the size of the diffusant. Diffusion constants measured for smaller molecules (< 1 kDa) are about fourfold smaller in cytoplasm than in water (9), which does not affect our calculation of millisecond diffusion timescales over bacterial cell lengths. We also assume all enzyme-catalyzed reactions have first-order kinetics, i.e. substrate concentrations are substantially lower than Michaelis constants ($[S] \ll K_M$). These assumptions give the following equations:

$$\begin{aligned}\frac{dC_{in}}{dt} &= \alpha(C_{out} - C_{in}) - \gamma C_{in} - (\delta C_{in} - \phi H_{in}) \\ \frac{dH_{in}}{dt} &= \beta(H_{out} - H_{in}) + (\delta C_{in} - \phi H_{in})\end{aligned}$$

Here we treat both CO₂ and HCO₃⁻ as entering the cell passively with “effective permeabilities” α and β . These effective permeabilities account for the surface area to volume ratio of bacterial cells, which, for rod shaped cells around the size of *E. coli*, is $SA/V \approx 4 \mu\text{m}^{-1}$ (BNIDs [101792](#) and [114924](#)) as we discuss below.

γC_{in} is a linearized expression for rate of irreversible CO₂ fixation by rubisco, where $\gamma = k_{cat}[rubisco]/K_M$ assuming a Michaelis-Menten formalism and $C_{in} \ll K_M$. In contrast to rubisco, the CA reaction is reversible. As such, $(\delta C_{in} - \phi H_{in})$ the balance of the rates of CO₂ hydration (δC_{in}) and HCO₃⁻ dehydration (ϕH_{in}), assuming each of these reactions are in their linear regimes as well. While the assumption of linearity is not required, it is also not counterfactual: typical K_M values measured for bacterial rubiscos (11) and carbonic anhydrases (12) are comparable to equilibrium concentrations of CO₂ and HCO₃⁻ in water in equilibrium with ambient air at 25 C (Figure S11).

We set both derivatives to 0 and solve for the steady-state values of C_{in} and H_{in}.

$$C_{in} = \frac{C_{out}(K_{EQ}\beta\phi + \alpha(\beta + \phi))}{\beta(\alpha + \gamma + \delta) + \phi(\alpha + \gamma)}$$

$$H_{in} = \frac{C_{out}(\alpha\delta + K_{EQ}\beta(\alpha + \gamma + \delta))}{\beta(\alpha + \gamma + \delta) + \phi(\alpha + \gamma)}$$

If we further assume that CA activity is negligible, i.e. that $\delta, \phi \approx 0$, then we recover the solution from our simplified main-text calculation where $C_{in} = \frac{C_{out}\alpha}{\alpha + \gamma}$ is independent of H_{in} . As a reminder, we used this equation to calculate that $C_{in} > 0.9C_{out}$ in the absence of CA activity, even when rubisco comprises 20% of total protein.

The above calculation implies that CA expression could increase C_{in} by at most 10% because CAs are not coupled to any energy source and, therefore, cannot increase C_{in} above C_{out} . This calculation depends, of course, on the rubisco kinetics and expression (γ) and membrane permeability to CO_2 (α). Rubisco kinetics have been studied in great depth and are well-constrained (11, 13). Similarly, many generations of physical chemists have studied the permeability of lipid membranes to small molecules and developed theory to estimate membrane permeabilities (14–16). Nonetheless, membrane permeabilities can depend on the lipid composition of the membrane and the complement of protein channels embedded therein (17).

Assuming that rubisco fixation is the sole growth-limiting reaction, we can estimate the exponential growth rate from C_{in} by calculating the rubisco fixation rate $\gamma C_{in} \approx 9 \times 10^3 \mu\text{M/s}$. Here we took $C_{out} \approx 10 \mu\text{M}$, which is roughly Henry's law equilibrium with present-day atmosphere at 25 °C (Fig. S16), $\alpha = 10^4 \text{ s}^{-1}$ and $\gamma = 10^3 \text{ s}^{-1}$. We expound on this choice of values in the main text and below. Assuming a cell volume of $\approx 1 \text{ fL}$ (BNIDs [104843](#), [100004](#)), $9 \times 10^3 \mu\text{M/s}$ equals a fixation rate of roughly $5 \times 10^6 \text{ CO}_2/\text{s}$ or $\approx 10^{10} \text{ CO}_2/\text{hr}$. An *E. coli* cell of this volume contains $\approx 10^{10}$ carbon atoms (BNID [103010](#)) and Cyanobacteria do not differ substantially from *E. coli* in carbon content (compare BNIDs [105530](#) and [111459](#)). Therefore, assuming no loss of fixed carbon, such a Cyanobacterium would double once an hour. Autotrophic respiration, which equals the difference between gross and net fixation, is typically less than 50% of gross both in pure cyanobacterial cultures (18) and natural ecosystems (19) implying a doubling time of at most 2 hours.

Given the model articulated above, a 10% increase in C_{in} (e.g. due to CA expression) can increase the rubisco carboxylation rate by at most 10%. As rubisco is required for producing all biomass carbon in autotrophy, a 10% increase in the rate of rubisco carboxylation can increase the exponential growth rate by at most 10%. However, in Figures S5-6 the “rubisco alone” strain did not meaningfully grow in 0.5% CO_2 while the strains expressing a CA or Ci transporter grew robustly. These qualitative effects indicated that we should look for a mechanism that can improve growth by more than $\approx 10\%$. As described in the main text and the following section, the cellular demand for HCO_3^- , which is required for several anabolic carboxylation reactions (20–23), is one such mechanism.

Notably, CO_2 and HCO_3^- do interconvert spontaneously. The spontaneous reaction is associated with

relatively slow kinetics, with $\delta_{spont} \approx 10^{-2} s^{-1}$ and $\phi_{spont} \approx 4 \times 10^{-3} s^{-1}$ near pH 7 (7, 24). Therefore, zero CA expression does not entail our above assumption that $\delta, \phi \approx 0$. Rather, to recover the expression for C_{in} above, we require that $\phi_{spont} \ll \beta$, $K_{EQ} \phi_{spont} \ll \alpha$, and $\delta_{spont} \ll \gamma = k_{cat}[rubisco]/K_M$. The latter is true for any modest level of rubisco expression: as typical rubiscos have $k_{cat}/K_M \approx 10^5 M^{-1} s^{-1}$ (11) and a bacterial rubisco should have a concentration of at least $10^{-6} M$ (25), $\gamma \geq 10 s^{-1} \gg \delta_{spont}$ (Fig. S11). Similarly, $\beta = SA \times P_H/V \approx 10^{-2} s^{-1}$ is roughly five times larger than ϕ_{spont} near pH 7 (7). Finally, near pH 7, $K_{EQ} \approx 10$ and so $K_{EQ} \phi_{spont} \approx 4 \times 10^{-2} s^{-1}$. This value is similar in scale to β , which is 2-3 orders smaller than α (7). Therefore, the simplified equation above is supported near pH 7.

A model of autotrophy including the HCO_3^- -dependence of growth

Our above calculation indicated to us that CA cannot act as a CO_2 pump and that, therefore, some factor is missing from the naive model of autotrophy given above. We assume that the missing factor is the ubiquitous dependence of microbial growth on HCO_3^- . This dependence is well-documented for heterotrophic microbes, which require carbonic anhydrases for growth in ambient air (4, 5, 20–22, 26) and is argued to stem from the reliance on HCO_3^- dependent carboxylases in nucleotide, amino acid, and lipid biosynthesis (20–22). This view is supported by simple chemical logic: CO_2 is very cell-permeable (see discussion below), so it is unlikely that CO_2 is growth-limiting when available extracellularly. Experiments in yeast (21) and *S. pneumonia* (22) provide further support, showing that supplementing the growth media with the products of these carboxylation reactions (e.g. fatty acids) rescues growth in ambient air. Moreover, recent experiments show that ambient air growth of an *E. coli* CA mutant is rescued when a Cyanobacterial $Na^+ : HCO_3^-$ symporter, *sbtA*, is expressed (27, 28). Similar CA dependencies have been observed in land plants (23) and manually-curated metabolic models of autotrophs include these same carboxylation reactions (23, 29, 30), indicating that this dependence of growth on HCO_3^- is very widespread, perhaps even universal.

The primary enzymology research supporting the use of HCO_3^- as the carboxylation substrate by pivotal anabolic enzymes is extensive. Biotin-dependent carboxylases like acetyl-CoA carboxylase (producing malonyl-CoA to initiate fatty acid biosynthesis) and pyruvate carboxylase (the primary anaplerotic carboxylase in many organisms) are known to use HCO_3^- as part of a multi-step mechanism (31, 32). Carbamoyl phosphate synthetase generates carbamoyl-P for arginine and bacterial biosynthesis from HCO_3^- , an amine donor (ammonia or glutamate), and 2 ATP (33). Purine biosynthesis likewise requires a carboxyl donor to generate 4-carboxyaminoimidazole ribonucleotide. In bacteria this reaction is typically catalyzed by a pair of enzymes, *purE* and *purK*, which utilize HCO_3^- (34, 35), while eukaryotes typically rely on a “class II” *purE* for which is considered to use CO_2 (21, 35).

Our experiments demonstrate that both CCMB1 *E. coli* and the model facultative chemolithoautotroph *C. necator* depend on CA for robust rubisco-dependent growth in intermediate CO_2 levels (0.5% and

1.5%, Fig. 5). Note that *C. necator* was grown in autotrophic conditions in Figure 5, with H₂ being the electron donor and CO₂ being the only carbon source (*Methods*). As the *C. necator* growth defect was fully reversed by expression of the DAB2 Ci transporter (Figures 5), which is understood to produce intracellular HCO₃⁻ by vectorial hydration of extracellular CO₂, we interpret these data as supporting the hypothesis that *C. necator* depends on intracellular HCO₃⁻ for autotrophic growth in ambient air.

We therefore augmented our model to reflect the apparent ubiquity of bicarbonate dependence by including (i) an HCO₃⁻ consuming flux, $-\omega H_{in}$, representing bicarbonate-dependent carboxylation in central metabolism (henceforth “bicarboxylation”) and (ii) a flux, $+\chi H_{out}$, producing intracellular HCO₃⁻ representing energized bicarbonate uptake systems like the DABs (36) or Cyanobacterial *sbtA* transporters (27, 37).

$$\begin{aligned}\frac{dC_{in}}{dt} &= \alpha(C_{out} - C_{in}) - \gamma C_{in} - (\delta C_{in} - \phi H_{in}) \\ \frac{dH_{in}}{dt} &= \beta(H_{out} - H_{in}) + (\delta C_{in} - \phi H_{in}) + \chi H_{out} - \omega H_{in}\end{aligned}$$

Following the example of the Farquahar model of photosynthesis (38), we assume that the flux to biomass J_B is determined as the minimum of two fluxes: the CO₂-dependent flux through rubisco (γC_{in}) and flux through HCO₃⁻ dependent carboxylation reactions (ωH_{in}). This is co-limitation expressed as $J_B = \min(\gamma C_{in}, \omega H_{in} / q)$ where q is the fraction of biomass carbon deriving from HCO₃⁻. The exponential growth rate λ can be estimated from J_B by noting that a typical bacterial cell contains $\approx 10^{10}$ carbon atoms ([BNID 103010](#)). For simplicity we ignore the carbon cost of cellular maintenance, though this could be included in future renditions of the model.

Steady-state solutions are given below. These values determine the steady-state rates of rubisco carboxylation and bicarboxylation, which, in turn, determines the biomass production flux and exponential growth rate.

$$\begin{aligned}C_{in} &= \frac{C_{out}(K_{EQ}\phi(\beta + \chi) + \alpha(\beta + \phi + \omega))}{\beta(\gamma + \delta) + \gamma\phi + \omega(\gamma + \delta) + \alpha(\beta + \phi + \omega)} \\ H_{in} &= \frac{C_{out}(\alpha\delta + K_{EQ}(\alpha + \gamma + \delta)(\beta + \chi))}{\beta(\gamma + \delta) + \gamma\phi + \omega(\gamma + \delta) + \alpha(\beta + \phi + \omega)}\end{aligned}$$

It is evident from these expressions that the rate of biomass production $J_B = \min(\gamma C_{in}, \omega H_{in} / q)$ will depend on H_{in} in some circumstances and on C_{in} in others. For example, if we assume $\delta, \phi, \chi \approx 0$, we find $H_{in} = C_{out} K_{eq} \beta / (\beta + \omega)$. Therefore, if CA and Ci uptake activities are negligible and the HCO₃⁻ permeability β is much smaller than the bicarboxylation activity ω , H_{in} will be small and growth will be limited by low bicarboxylation flux. In the following sections we describe how we set reasonable ranges for all model parameters in order to examine the dependence of autotrophic biomass production on the activity of rubisco, CA, and Ci uptake systems.

Choosing realistic ranges for parameter values

We assume the pH is the same both inside and outside the cell for simplicity. Furthermore, we choose pH 7.1 since the effective pK_a between CO_2 and HCO_3^- is roughly 6.1 in biological salt concentrations (see supplement of (7) for detail). According to the Henderson-Hasselbalch relation, $\text{pH} = pK_a + \log_{10}([\text{HCO}_3^-]/[\text{CO}_2])$, so the choice of $\text{pH} = 7.1$ sets the equilibrium constant $K_{\text{EQ}}(\text{pH}) = [\text{HCO}_3^-]/[\text{CO}_2] = 10^1$ both inside and outside the cell (7).

Since we endeavor to explain phenotypes observed in relatively low CO_2 levels (e.g. ambient air in Fig. 6 and 0.5-1.5% CO_2 in Figs. 4-5), we assume the extracellular CO_2 concentration is in Henry's law equilibrium with present day atmosphere ($\approx 0.04\%$ CO_2). This gives $C_{\text{out}} \approx 15 \mu\text{M}$ (7, 39) and, with $K_{\text{EQ}} = 10$, $H_{\text{out}} = 150 \mu\text{M}$ (Fig. S16). For the permeability of the cell membrane to CO_2 and HCO_3^- , we use $P_c = 3 \times 10^3 \mu\text{m/s}$ and $P_H = 10^{3.2-\text{pH}} \times 30 \mu\text{m/s} \approx 4 \times 10^{-3} \mu\text{m/s}$ following (7). The latter relation calculates the permeability of HCO_3^- from its pH-dependent abundance and the permeability of H_2CO_3 , assuming that HCO_3^- has negligible permeability when compared to H_2CO_3 due to its charge. This calculation is described in detail in the supplement of (7). We multiply these permeabilities by the surface area to volume ratio $SA/V \approx 4 \mu\text{m}^{-1}$ to obtain estimates of $\alpha \approx 1.2 \times 10^4 \text{ s}^{-1}$ and $\beta \approx 1.6 \times 10^{-2} \text{ s}^{-1}$.

We are left to choose ranges for the enzymatic activity parameters γ , δ , ϕ , ω and χ . First, we note that the the CA activity parameters δ and ϕ must be consistent with the equilibrium constant K_{EQ} (i.e. must obey the Haldane relation). If the CA reaction was allowed to equilibrate, it would carry no net flux and $\delta C_{\text{in}} - \phi H_{\text{in}} = 0$. In these conditions $K_{\text{EQ}} = \frac{H_{\text{in}}}{C_{\text{in}}} = \frac{\delta}{\phi}$, giving $\phi = \frac{\delta}{K_{\text{EQ}}}$.

To set ranges for enzyme activities γ (rubisco carboxylation) and δ (CO_2 hydration by CA), we reviewed literature values for k_{cat}/K_M for rubiscos (11) and CA (12, 40). The geometric mean of measured rubisco k_{cat}/K_M values is $\approx 0.2 \mu\text{M}^{-1} \text{ s}^{-1}$ with a multiplicative standard deviation of roughly two-fold (Figure S11). A typical protein concentration might range between 0.1 and 100 μM (25). As rubisco is typically one of the most abundantly expressed proteins in autotrophic cells (41), we extend this range to 0.1 μM - 1 mM implying that γ ranges from $\approx 10^2$ - 10^3 s^{-1} . Note that we are using μM units for both the enzyme and substrate so that γC_{in} has units of $\mu\text{M/s}$ carbon consumed. For CA, the geometric mean k_{cat}/K_M value in the direction of CO_2 hydration is $\approx 20 \mu\text{M}^{-1} \text{ s}^{-1}$ with a multiplicative standard deviation of roughly seven-fold (Figure S11). CA is not typically as highly-expressed as rubisco, so a plausible range for δ is perhaps 0.1- 10^4 s^{-1} when a CA is expressed. As noted above, the spontaneous reaction is characterized by $\delta_{\text{spont}} \approx 10^{-2} \text{ s}^{-1}$.

When environmental CO_2 concentrations are sufficiently high, rubisco and CA can become CO_2 saturated and our assumption of linear kinetics is violated as enzymatic rates become zero order (i.e. independent of substrate concentrations C_{in} and H_{in}). This can be addressed by a simple modification of the model, setting the rubisco rate to $k_{\text{cat}} [\text{rubisco}]$ and the CA rate to $(k_{\text{cat,H}} - k_{\text{cat,D}})[\text{CA}]$ as appropriate. Here $k_{\text{cat,D}}$ is the k_{cat} in the direction of CO_2 hydration and $k_{\text{cat,D}}$ is calculated from $k_{\text{cat,H}}$ via the Haldane relation as

described above. This latter relation supposes that CA is substrate-saturated in both hydration and dehydration directions, i.e. saturated by CO_2 and HCO_3^- both. When such a model is appropriate, realistic k_{cat} values are required. Figure S11 shows that rubisco k_{cat} values range from roughly $1\text{-}10\text{ s}^{-1}$ (geometric mean 3.3 s^{-1} with a multiplicative standard deviation of 1.5 fold) and k_{cat} values for CA-catalyzed CO_2 hydration range from $\approx 10^4\text{-}10^6\text{ s}^{-1}$ (geometric mean $1.3 \times 10^5\text{ s}^{-1}$ with a multiplicative standard deviation of 6.4 fold).

Only ω and χ remain to be set. We chose $\omega = \gamma / q$ with $q = 100$ to reflect our assumption that both rubisco and bicarboxylation processes contribute to biomass production in a roughly fixed proportion (q), but that rubisco is responsible for the production of nearly all biomass carbon in autotrophy (we assume 99%) and bicarboxylation is responsible for the remainder (1%). We used the same value of q in calculating the biomass flux from the principle of co-limitation, i.e. $J_B = \min(\gamma C_{in}, \omega H_{in} / q)$. This amounts to assuming that the cell regulates the bicarboxylation and rubisco capacities to match their relative contributions to biomass production. Our assumption that ω is proportional to γ can be omitted, but this yields a model with an additional free parameter that is challenging to constrain from data.

To set χ , we consider measurements of saturated C_i uptake rates in Cyanobacteria, which are on the order of $10\text{-}100\text{ }\mu\text{mol}$ per mg chlorophyll per hour (42). Since a typical cyanobacterial cell contains $\approx 10^{-11}$ mg chlorophyll (43), the per-cell rates are at most $10^{-9}\text{ }\mu\text{mol}/\text{hour}$, or $3 \times 10^{-13}\text{ }\mu\text{mol}/\text{s}$ into a volume of $\approx 1.5\text{ }\mu\text{m}^3 = 1.5 \times 10^{-15}\text{ L}$. Uptake rates in this range would contribute $\approx +200\text{ }\mu\text{M}/\text{s}$ to dH_{in}/dt . If $\chi H_{out} \leq 200\text{ }\mu\text{M}/\text{s}$ and $H_{out} = 100 - 2000\text{ }\mu\text{M}$ depending on the pH then $\chi \leq 2\text{ s}^{-1}$. Note that Figure 7 and S12-15 use wider ranges for γ , δ and χ than calculated here in order to illustrate the behavior of the model with two-dimensional plots.

On the requirement for bicarbonate for biosynthesis

One way to examine the role of bicarbonate dependent carboxylation in our model is to set the bicarboxylation rate constant $\omega = 0$. This gives

$$C_{in} = \frac{C_{out}(\alpha(\beta + \phi) + K_{EQ}\phi(\beta + \chi))}{\beta(\alpha + \gamma + \delta) + \phi(\alpha + \gamma)}$$

$$H_{in} = \frac{C_{out}(\alpha\delta + K_{EQ}(\alpha + \gamma + \delta)(\beta + \chi))}{\beta(\alpha + \gamma + \delta) + \phi(\alpha + \gamma)}$$

We see that C_{in} and H_{in} remain interdependent, i.e. the processes that produce H_{in} like CO_2 hydration by carbonic anhydrase (δ) and active C_i uptake (χ) are represented in the equation for C_{in} and vice versa. Nonetheless, these processes have negligible effect on CO_2 fixation by rubisco because (i) C_{in} uniquely determines the rubisco rate in our model, and (ii) literature values for CO_2 permeability are high enough that (iii) rubisco cannot reduce C_{in} much beneath C_{out} , as described above. Figures S13 and S15 illustrate this point by showing that order-of-magnitude changes to δ , χ and γ do not substantially affect C_{in} . In particular, in Figure S13A, $C_{in} \approx C_{out}$ until rubisco activity reaches very high levels $\gamma \approx 10^4\text{ s}^{-1}$. As a result, the carboxylation flux increases with the rubisco activity γ , but is unaffected by CA activity δ (Figure

S13G). This is a simple consequence of the fact that the measured CO_2 permeability of biological membranes (α) is quite high. Figure S14 illustrates this point using a model with substantial Ci uptake activity ($\chi = 100 \text{ s}^{-1}$) and an unrealistically low value of $\alpha = 12 \text{ s}^{-1}$ (1000-fold smaller than we estimated above). Very low α values enable CA and Ci uptake to act in concert to pump CO_2 into the cell by (i) actively taking up HCO_3^- , and (ii) converting HCO_3^- into CO_2 via CA, which is (iii) retained in the cell when the membrane permeability to CO_2 (α) is much smaller than calculated or measured (14, 16).

If order-of-magnitude changes to δ and χ do not affect C_m (when realistic α values are used), then the rubisco carboxylation flux cannot change and we must invoke another mechanism to explain the observed phenotypes. As discussed in the main-text and above, we assumed that the ubiquitous requirement for HCO_3^- as the substrate for biosynthetic carboxylases is the underlying mechanism. Once we described the growth rate as mathematically coupled to both rubisco carboxylation of CO_2 and biosynthetic carboxylation of HCO_3^- , we found that changes in CA and Ci uptake activities do produce changes in growth (Figure S13).

A quantitative view of futile cycling

Figures 7C and S15 document the effects of simultaneously varying CA activity (δ) and Ci uptake (χ) on the co-limitation model of autotrophic growth, showing that futile cycling only occurs when both activities are present at high levels. As discussed in the main-text, this quantitative view helped us understand why co-expression of CA and Ci uptake activities was not deleterious to CCMB1 or *C. necator* (Figures 4-5), but rather beneficial to CCMB1, enabling modest growth in ambient air (Figure 6). This understanding relies on a fundamental difference between CA and Ci uptake: that Ci uptake is energized and can work against equilibrium, while CAs are not coupled to any energy source and cannot.

Given that CAs are not energy-coupled, they cannot cause any leakage or futile cycling on their own. This is clearly seen by considering Figure 7C or the bottom row of S15: if CA activity δ was increased while Ci uptake χ is kept low, the modeled cell did not leak Ci. At best, CA expression can lead to equilibration of the Ci pools on both sides of the membrane (Figure S15A-B). Based on a variety of experiments, Ci uptake systems are considered to use energy to concentrate HCO_3^- in the cytoplasm either by pumping extracellular HCO_3^- or by energy-coupled hydration of CO_2 at the cell membrane. The energy sources used range from ATP to redox and ion gradients (36, 44, 45). Regardless of the underlying mechanism, our current understanding of the CCM requires a high intracellular HCO_3^- concentration that is, crucially, not in equilibrium with CO_2 (7, 46, 47). This is understood to be the reason that expression of cytoplasmic CA activity is highly deleterious to photosynthesis and growth in model Cyanobacteria (46).

Energy-coupled Ci uptake can therefore concentrate HCO_3^- in the cytosol and HCO_3^- spontaneously dehydrates to CO_2 on a timescale of $\approx 10 \text{ s}$ (7, 24). High χ values can therefore produce Ci leakage on their own, which can be seen in Figure 7C and S15 where very high χ values lead to both CO_2 and HCO_3^- leakage, i.e. $J_{L,B}, J_{L,H} > 0$. Leakage of CO_2 indicates that some HCO_3^- dehydrates to CO_2 , some of which can be used by rubisco. This effect is amplified by CA expression: when δ was increased at high χ , zero leakage ($J_{L,tot} = J_{L,B} + J_{L,H} = 0$) could be achieved at relatively lower χ (Figure 7C and bottom row of S15)

without altering the flux to biomass (J_B) substantially (depicted in log-scale in Figure S15I). According to our model, therefore, modest co-expression of CA and Ci uptake can reduce energy expended on pumping and balance the supply of CO_2 and HCO_3^- with the cellular demand for rubisco and bicarboxylation flux.

When δ and χ were both set to high values, the model produced substantial futile cycling with $J_{L,tot} / J_B \approx 100$ in extreme cases. First note that these values of $\delta = \chi = 10^3 \text{ s}^{-1}$ are several orders higher than the upper bounds we estimated above. Nonetheless, we can ask whether such a leakage rate should be expected to be deleterious to growth by comparing the energy expended on Ci pumping and CO_2 fixation. Ci pumping consumes ≈ 1 ATP/carbon (7, 45) while CO_2 fixation in the Calvin-Benson-Bassham cycle consumes 2.3 ATP/carbon (48, 49). Therefore, $J_{L,tot} / J_B \approx 100$ implies that 40-50 times more cellular energy is expended on Ci pumping than on CO_2 fixation.

Supplementary Figures

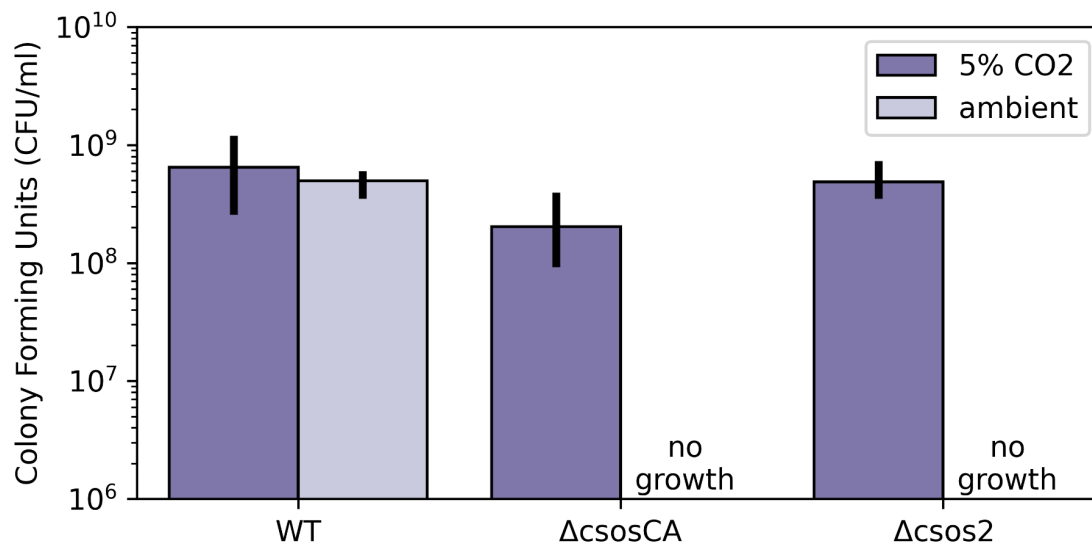


Figure S1: *H. neapolitanus* CCM mutants grow 5% CO₂ but not in ambient air. Quantification of panel B of Fig. 1. Wild-type *H. neapolitanus* (WT) grows well in 5% CO₂ (dark purple) and ambient air (0.04% CO₂, lighter purple), producing $> 10^8$ colony forming units per milliliter of culture in both conditions. Mutants lacking genes coding for essential CCM components grow in elevated CO₂ (dark purple) but fail to grow in ambient air (light purple). The $\Delta csosCA$ strain lacks the gene coding for the carboxysomal carbonic anhydrase (*csosCA*) while the $\Delta csos2$ strain lacks the gene coding for an unstructured protein, *csos2*, required for carboxysome formation (50, 51). These mutant strains both failed to grow in ambient air ("no growth"), but grew robustly in 5% CO₂ ($\approx 10^8$ colony forming units/ml). Bar heights give the mean of counts for three biological replicates, which each represent the mean of three technical replicates. Error bars give the standard deviation of the mean. See Table S4 for full description of strains and mutations.

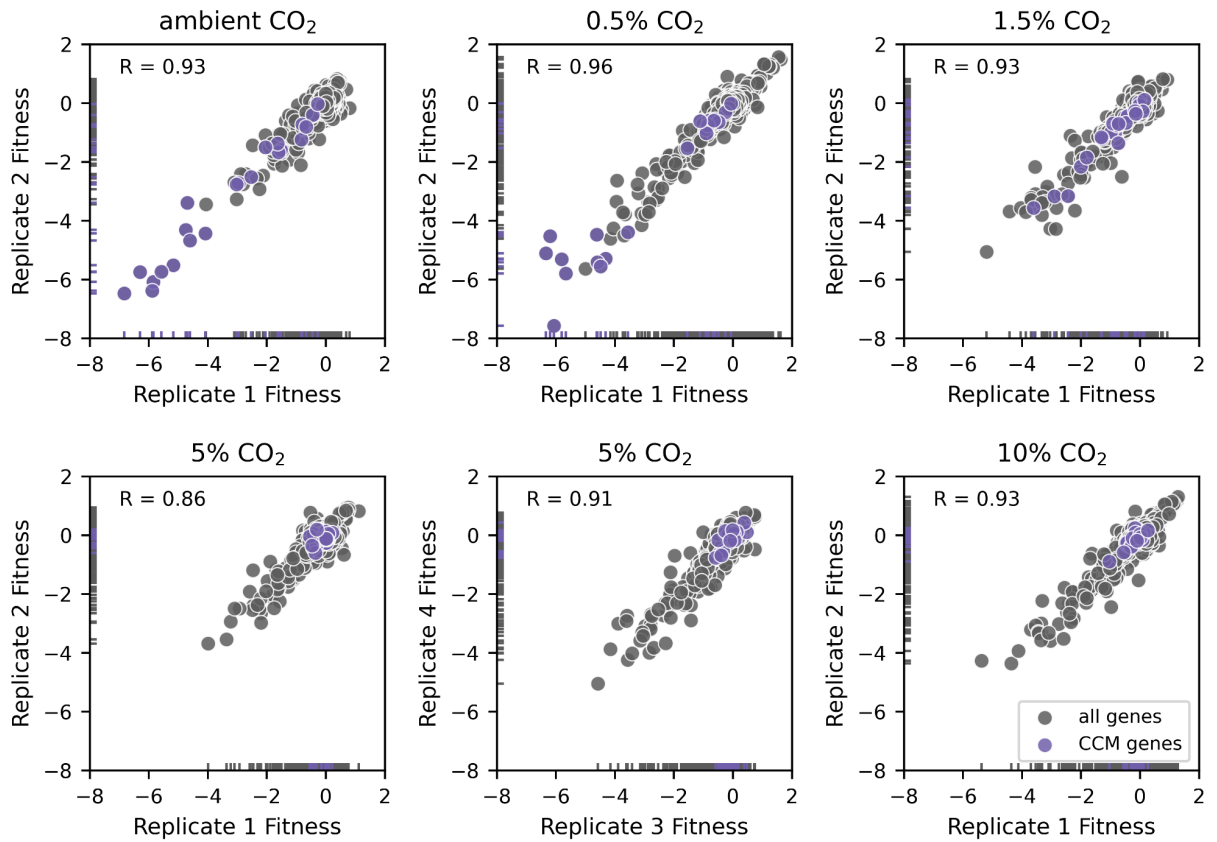


Figure S2: Reproducibility of *H. neapolitanus* fitness measurements across replicate experiments in the same CO₂ environment. All CO₂ conditions were assayed via duplicate cultures with biologically independent pre-cultures, except for the 5% CO₂ condition which was assayed in biological quadruplicate. Scatterplots show the correlation between replicates for those genes which produced high confidence fitness measurements in both replicates, with known CCM genes in purple and all other genes in grey. The Pearson correlation R is given for all pairs of replicates plotted and exceeds 0.85 in all cases. Marginal distributions of per-replicate fitness effects are given by the “rug” along the axes. As CCM gene disruptions (purple) represent the largest fitness effects observed in lower CO₂ conditions, the range of fitness effects decreases with increasing CO₂.

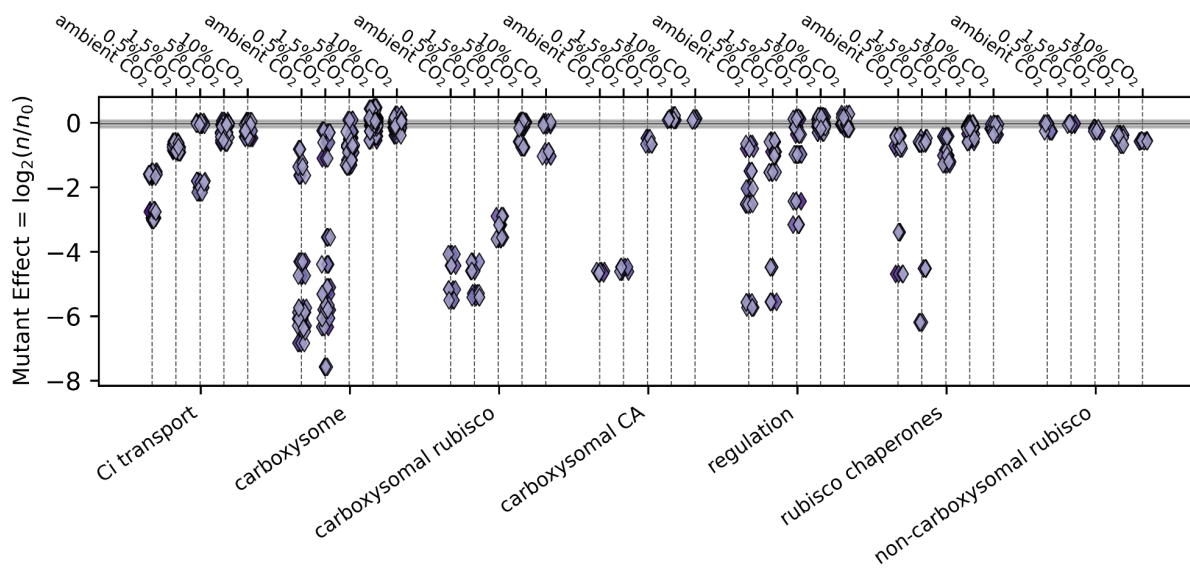


Figure S3: Contributions *H. neapolitanus* CCM genes to organismal fitness across five environmental CO₂ concentrations. As in Figure 2, data derive from batch competition assays of a barcoded whole-genome insertional mutagenesis library (RB-TnSeq) developed in (36). Data for ambient and 5% CO₂ conditions are reproduced from that reference, while data 0.5%, 1.5% and 10% CO₂ conditions were collected for this study. Each competition assay was performed in duplicate, except for the 5% CO₂ condition, which was performed in quadruplicate (i.e. biological duplicate in each study). We manually divided CCM-associated genes into several categories based on their known or presumed roles. The correspondence between genes and categories is given Table S1. The figure plots the fitness effects of knockouts for each gene category as a function of the CO₂ level and include three additional categories of genes omitted from Figure 2: putative transcriptional regulators of the CCM, rubisco chaperones, and the non-carboxysomal Form II rubisco (“non-carboxysomal rubisco”). The presence of a non-carboxysomal rubisco explains why mutations disrupting the carboxysomal enzyme are not very deleterious in 5-10% CO₂: the secondary rubisco is expressed in those conditions (52). The interpretation of fitness results is complicated by genetic redundancy for several other gene categories as well. For example, the *H. neapolitanus* genome encodes 6 carboxysome shell proteins, which differ in their abundances (53) and could have overlapping roles in the carboxysome structure (45, 54), which can cause polar effects where the knockout of an upstream gene has a larger effect due to perturbation of transcription of genes encoded downstream (55). Likewise, *H. neapolitanus* has two DAB-type Ci uptake complexes. These complexes are encoded by 2-3 genes each and are both functional when expressed in *E. coli* (36, 56), which may explain the complex CO₂-dependent phenotypes observed for “Ci transport” genes. The “regulation” and “rubisco chaperones” categories are more ad-hoc, as they group multiple genes with poorly-documented roles. Knockout of the rubisco chaperone acRAF, for example, is associated with sizable CO₂-dependent fitness defect, though it is as-yet unclear what role this gene plays in rubisco or carboxysome biogenesis in bacteria (1, 57).

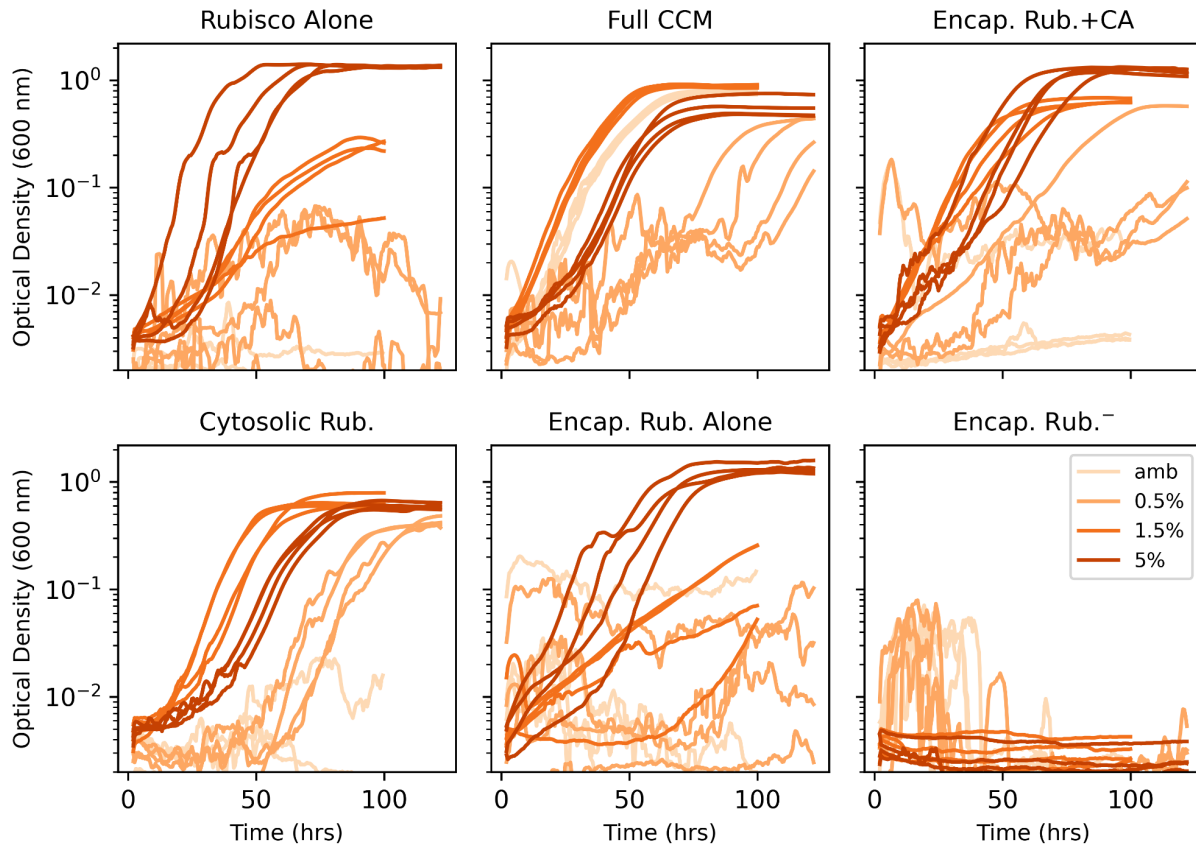


Figure S4: Growth curves testing the effect of rubisco encapsulation on the growth of CCMB1 in various CO₂ pressures. Each panel displays four biological replicate growth curves grown in four CO₂ pressures marked. The CO₂ pressure is denoted by the shade of orange in each panel. Figure 3 plots the endpoint densities of these curves (density at 100 hours). The CCMB1 *E. coli* strain grows in elevated CO₂ (1.5 and 5%) when rubisco is expressed (“Rubisco Alone”, top left). Expressing the full complement of CCM genes (“Full CCM”, top middle) permits growth in all CO₂ levels. Omitting the DAB-type Ci transporter from this construct (“Encap. Rub. + CA”, top right) nonetheless improves growth above the “Rubisco Alone” baseline in 0.5% and 1.5% CO₂. Mutating a single amino acid on rubisco (CbbL Y72R) eliminates carboxysome localization by abolishing CsoS2 binding (51). Introducing this mutation to a “Full CCM” construct (“Cytosolic Rub.”, bottom left) abolishes growth in atmosphere, as reported in (1), but not in 0.5% CO₂ or higher. Therefore, carboxysome localization of rubisco is not required for robust growth in 0.5% CO₂. Removing carboxysomal CA activity from the “Encap Rub. + CA” construct by active site mutation (CsoSCA C173S) abolishes the growth improvement observed when active CA is present (“Encapsulated Rub. Alone”, bottom middle). This result implies that the robust growth observed for “Cytosolic Rub.” and “Encap Rub.+CA” strains was due to the presence of carbonic anhydrase activity. A negative control strain carrying inactive rubisco (“Encap Rub.-”, CbbL K194M) fails to grow in any condition, as expected. See Table S4 for strains, Table S5 for plasmids and *Methods* for growth conditions.

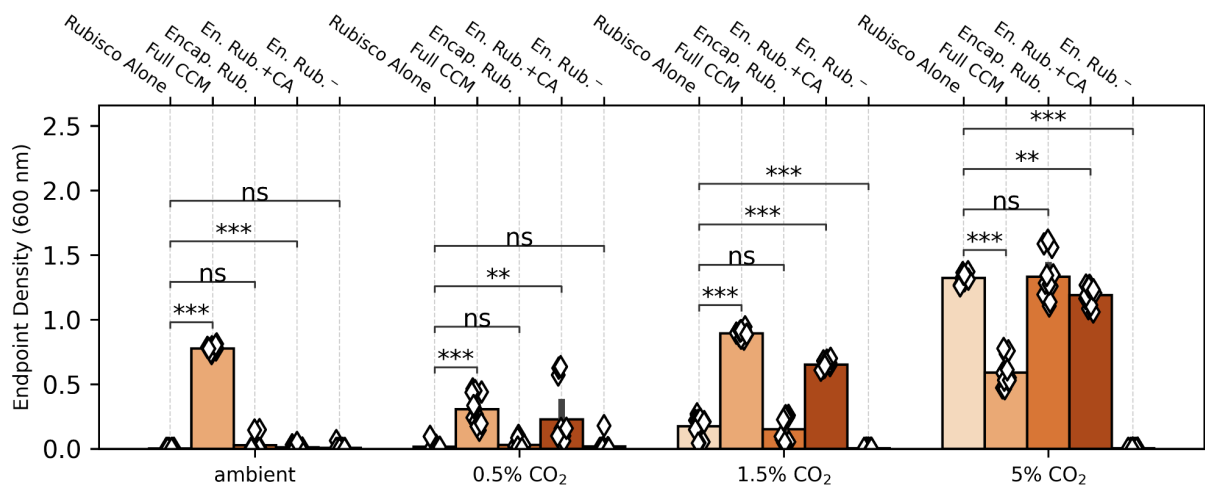


Figure S5: Assessment of statistical significance of differences in endpoint culture densities for CCMB1 strains testing rubisco encapsulation. Data and labels are identical to Figure 3, but reordered to group different strains grown in the same CO₂ condition. P-values were calculated by comparison to the 'Rubisco Alone' reference strain using a Bonferroni-corrected two-sided Mann-Whitney-Wilcoxon test. '*' denotes $p < 0.05$, '**' denotes $p < 0.01$, and '***' denotes $p < 0.001$. 'ns' denotes 'not significant' at the 5% threshold after Bonferroni correction.

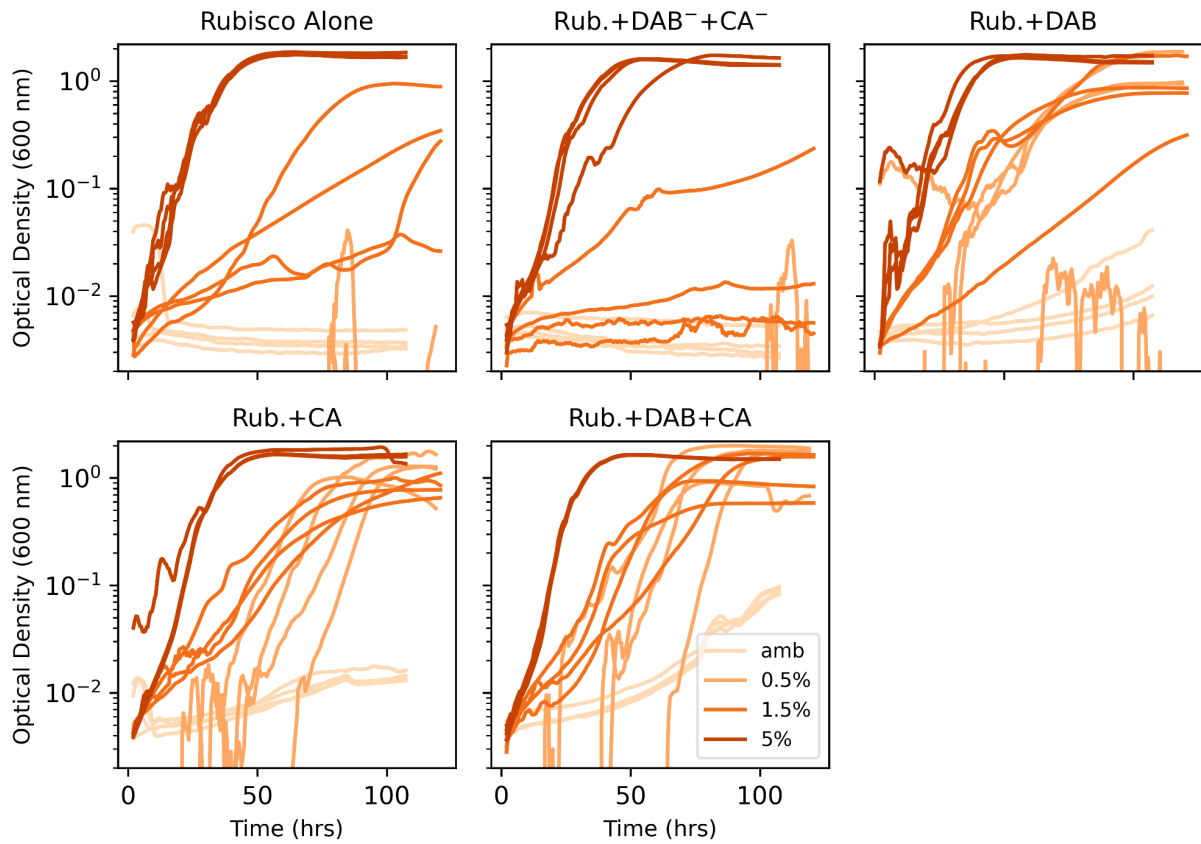


Figure S6: Growth curves testing the expression of CA and DAB-type Ci transporters on the growth of CCMB1 in various CO₂ pressures. Each panel displays four biological replicate growth curves grown in the four CO₂ pressures marked. pCO₂ pressure is denoted by the shade of orange in each panel. Labels are identical to Figure 4, which plots the endpoint densities of these curves (i.e. the density at 100 hours).

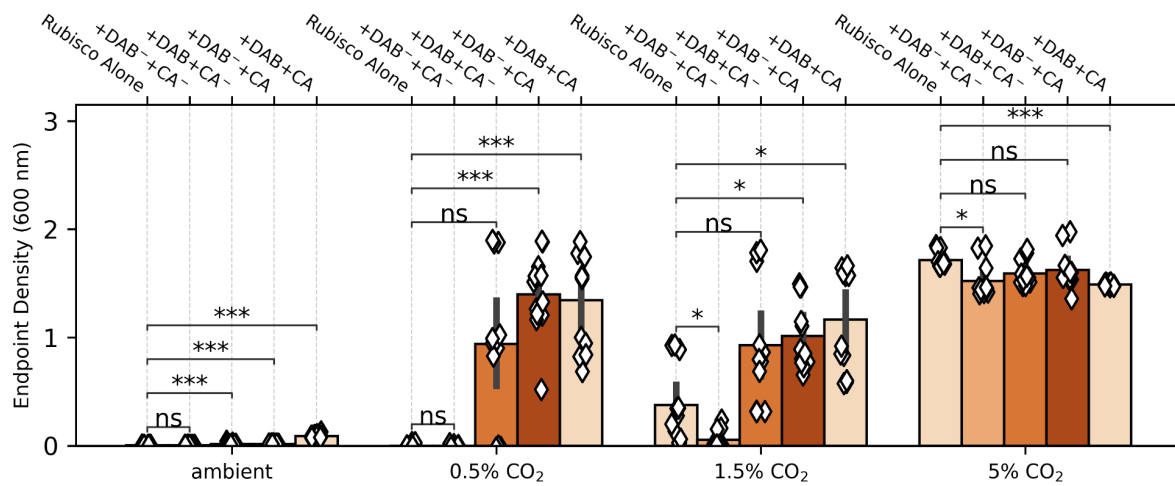


Figure S7: Assessment of statistical significance of differences in endpoint culture densities for CCMB1 strains testing expression of CA and DAB-type Ci transporters. Data and labels are identical to Figure 4, but reordered to group different strains grown in the same CO₂ condition. P-values were calculated by comparison to the 'Rubisco Alone' reference strain using a Bonferroni-corrected two-sided Mann-Whitney-Wilcoxon test. '*' denotes $p < 0.05$, '**' denotes $p < 0.01$, and '***' denotes $p < 0.001$. 'ns' denotes 'not significant' at the 5% threshold after Bonferroni correction.

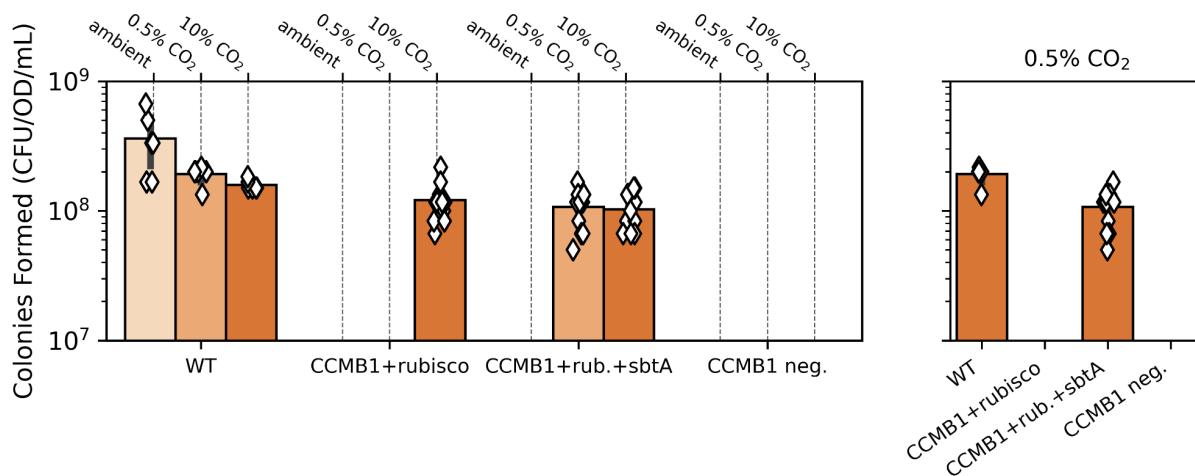


Figure S8: Expression of the cyanobacterial HCO_3^- transporter *sbtA* permits growth of rubisco-expressing CCMB1 in 0.5% CO_2 . Data give the number of colonies formed by each strain in three CO_2 conditions on M9 glycerol plates, where colony forming units were counted by plating tenfold serial dilutions of a pre-culture (grown in 10% CO_2) in each condition. Colony forming units (CFU) are reported per OD per mL of pre-culture to account for variation in the growth of the pre-culture. Wild-type, or WT, denotes *E. coli* BW25113, the parent strain of CCMB1. Here WT carries two vector control plasmids (pFE-sfGFP and pFA-sfGFP) so that it is resistant to the same antibiotics as the following CCMB1 strains. As expected, WT grows in all CO_2 levels tested. “CCMB1+rubisco” denotes CCMB1:p1A+pFA-sfGFP, where the p1A plasmid expresses the carboxysomal Form IA rubisco from *H. neapolitanus* and a cyanobacterial phosphoribulokinase (1). Consistent with Figures 3-4, this strain did not grow in 0.5% CO_2 but did grow in 10% CO_2 . “CCMB1+rubisco+sbtA” denotes CCMB1:p1A+pFA-sbtA, which expresses the cyanobacterial HCO_3^- transporter *sbtA* (27, 28, 45) on the pFA backbone. Comparing to the previous strain, it is clear that *sbtA* expression permitted growth in 0.5% CO_2 . This is highlighted by the right panel focusing on 0.5% CO_2 . “CCMB1 neg” denotes CCMB1:pFE-sfGFP+pFA-sfGFP. This strain does not express rubisco or phosphoribulokinase and fails to grow in all CO_2 conditions tested (similar to the rubisco point mutant “En. Rub” in Figure 3). Anhydrotetracycline (aTc) is used to induce expression from pFA and pFE plasmids; here all strains are induced with 100 nM aTc added to the agar plates (1). All CCMB1 strains failed to grow on plates lacking aTc induction (not shown).

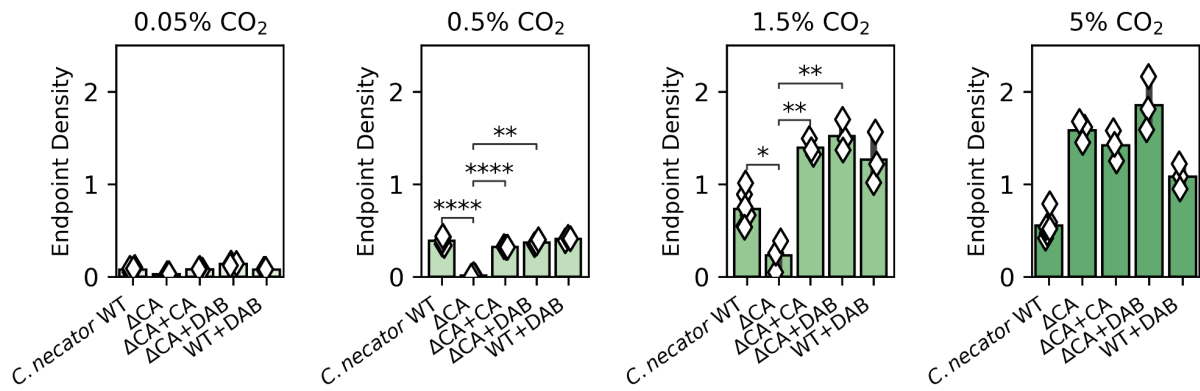


Figure S9: Assessment of statistical significance of differences in endpoint culture densities for *C. necator* strains testing expression of CA and DAB-type Ci transporters. Data and labels are identical to Figure 5, but reordered to group different strains grown in the same CO₂ condition. P-values were calculated by comparison to the 'Rubisco Alone' reference strain using a Bonferroni-corrected two-sided Mann-Whitney-Wilcoxon test. '*' denotes $p < 0.05$, '**' denotes $p < 0.01$, and '***' denotes $p < 0.001$. 'ns' denotes 'not significant' at the $P = 0.05$ threshold after Bonferroni correction.

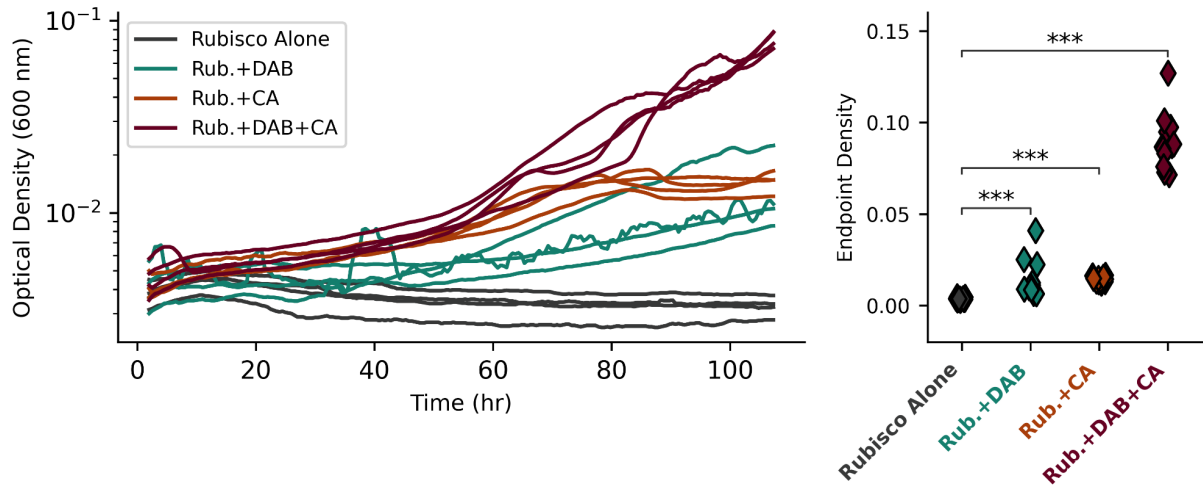


Figure S10: Growth curves and assessment of statistical significance for CCMB1 strains grown in ambient air. Left panel gives growth curves for 4 biological replicates of each strain described in Figures 4 and 6. The right panel compares the terminal optical densities for the four strains. P-values were calculated by comparison to the 'Rubisco Alone' reference strain using a Bonferroni-corrected two-sided Mann-Whitney-Wilcoxon test. '*' denotes $p < 0.05$, '**' denotes $p < 0.01$, and '***' denotes $p < 0.001$. 'ns' denotes 'not significant' at the 5% threshold after Bonferroni correction.

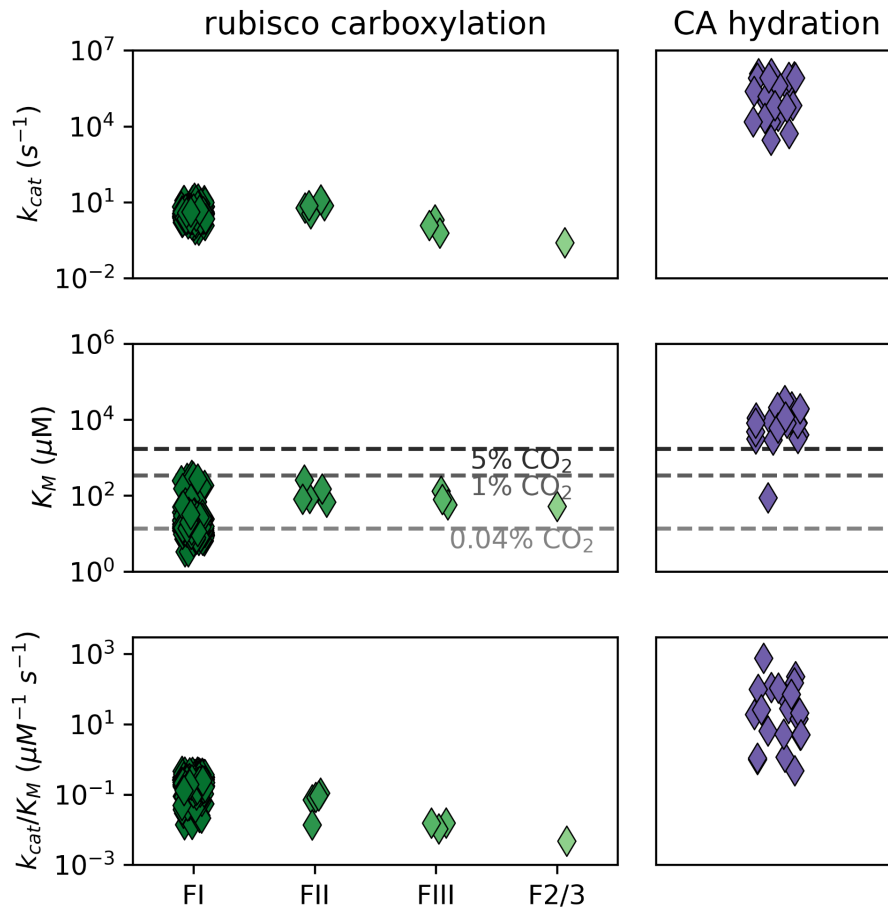


Figure S11: Literature values of rubisco and carbonic anhydrase kinetic parameters. In the Michaelis-Menten formalism (58, 59) the k_{cat} gives the substrate-saturated per-active site rate (top panels, s^{-1} units), the K_M denotes the substrate concentration at which an enzyme-catalyzed reaction achieves half the k_{cat} (middle panel, μM units) and k_{cat}/K_M gives the per-active site rate in the limit of low substrate concentrations ($[S] \ll K_M$). Rubisco data is drawn from (11) and CA data from (12). Carboxysomal rubiscos are of the form I (FI) variety that is also found in land plants (11, 45). The *H. neapolitanus* genome also encodes auxiliary form II (FII) rubisco. These isoforms typically have higher k_{cat} values, but also lower affinity towards CO₂, i.e. higher CO₂ K_M values than FI enzymes (60). Less data is available about the kinetics of Form III (FIII) and form II/III (F2/3) rubiscos (61). Notice that K_M values for FI rubiscos are comparable to CO₂ concentrations in water equilibrated with present day atmosphere at 25 °C, indicated by the dashed gray line marked 0.04% CO₂ (25). Similarly, K_M values associated with CA-catalyzed hydration of CO₂ greatly exceed the equilibrium CO₂ concentrations. Less data is available about the kinetics of Form III (FIII) and form II/III (F2/3) rubiscos (61). The empirical median k_{cat}/K_M value is $0.2 \mu M^{-1} s^{-1}$ (interquartile range $0.17-0.27 \mu M^{-1} s^{-1}$) for FI rubiscos and $20 \mu M^{-1} s^{-1}$ for CA catalyzed hydration of CO₂ (interquartile range $5-98 \mu M^{-1} s^{-1}$).

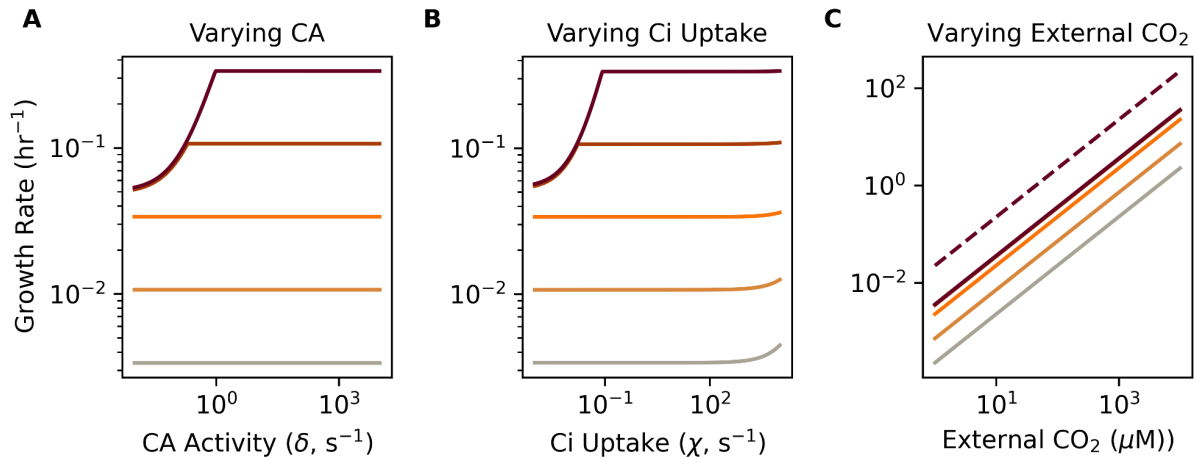


Figure S12: The effects of individually varying CA activity (δ), Ci uptake (χ), and the extracellular CO_2 concentration (C_{out}) on growth in the co-limitation model of autotrophic growth. Panel (A) is identical to main text Figure 7B showing that the model exhibits two regimes: one wherein growth is limited by rubisco flux and another where it was limited by bicarboxylation flux. At low rubisco levels (lighter-colored lines), growth is rubisco-limited: increasing rubisco activity (darker lines) produced faster growth, but the growth rate was insensitive to increasing δ because slow CO_2 hydration provided sufficient HCO_3^- to keep pace with rubisco. At higher rubisco levels (maroon lines), growth was bicarboxylation-limited and increasing δ was required for increasing rubisco activity to translate into faster growth. (B) Varying Ci uptake activity χ led to similar effects. As we assume a spontaneous level of CO_2 hydration even in the absence of CA ($\delta = 10^{-2} \text{ s}^{-1}$), very high χ values can increase growth by producing CO_2 for rubisco in the rubisco-limited regime. This phenomenon is only apparent at when χ is implausibly large and the rubisco activity γ is small, but is nonetheless instructive for understanding the distinctions between CA and energized Ci uptake. (C) As our co-limitation model is linear, varying the external CO_2 concentration produces a proportional increase in the rubisco flux. Additionally, because we assume extracellular HCO_3^- and CO_2 are in equilibrium with respect to the pH, H_{out} increases proportionally with C_{out} and supplies sufficient HCO_3^- by passive diffusion and spontaneous hydration of CO_2 . However, notice that growth does not increase in proportion with rubisco activity as in panels A-B (solid lines represent γ values evenly-spaced on a log scale) because, at higher $\gamma = q\omega$ values, passive diffusion and spontaneous hydration of CO_2 are insufficient to supply HCO_3^- required for a proportional increase. This can be seen by considering the difference between the solid maroon line (CA $\delta = 10^{-2} \text{ s}^{-1}$) and the dashed one ($\delta = 10^{-1} \text{ s}^{-1}$).

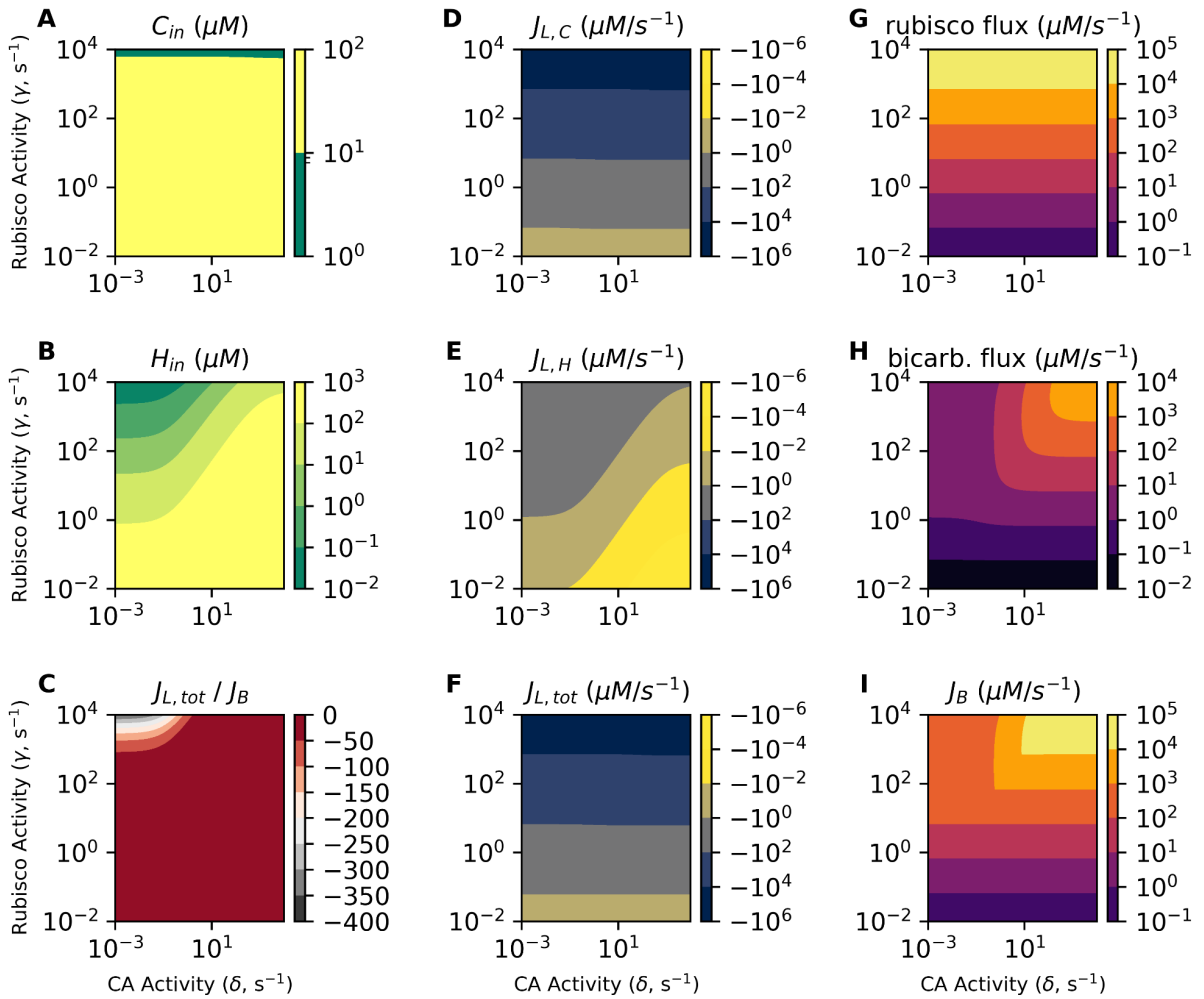


Figure S13: Rubisco and bicarboxylation-limited growth regimes in the co-limitation model. In each panel, the x-axis gives the CA activity δ in s^{-1} units and the y-axis the rubisco activity γ in the same units. Color in the filled contour plots gives the quantity named in each panel title. We set CO_2 permeability $\alpha = 1.2 \times 10^4 s^{-1}$ and HCO_3^- permeability $\beta = 1.5 \times 10^2 s^{-1}$ as calculated in the supplementary text. The C_i uptake activity χ was set to 0 for all panels. (A-B) C_{in} and H_{in} are the intracellular CO_2 and HCO_3^- concentrations, respectively. Notice that C_{in} varies little over orders of magnitude changes in γ and is independent of CA activity δ as discussed in the main text. (D-E) $J_{L,C} = -\alpha(C_{out} - C_{in})$ and $J_{L,H} = -\beta(H_{out} - H_{in})$ represent the flux of CO_2 and HCO_3^- leakage from the cell. $J_{L,C}$ is positive when $C_{in} > C_{out}$ and negative when $C_{in} < C_{out}$ and there is net passive diffusion of CO_2 into the cell. As we set $\chi = 0$, both leakage fluxes are uniformly negative here, connoting passive uptake of both CO_2 and HCO_3^- . (F) $J_{L,tot} = J_{L,C} + J_{L,H}$ is the total flux of C_i leakage from the cell. Notice that $J_{L,H}$ contributes negligibly to $J_{L,tot}$ here because no HCO_3^- is pumped when $\chi = 0$. (G) The rubisco carboxylation flux is calculated as γC_{in} . Given these permeability values, the rubisco flux is independent of CA activity (δ , x-axis) because passive diffusion of CO_2 across the membrane is sufficient to supply even very high rubisco activities (γ , y-axis). In contrast, panel (H) gives the bicarboxylation flux ωH_{in} , which varies with both δ and γ . The dependence on γ is an artifact of our assumption that bicarboxylation capacity ω is proportional to γ . The dependence on δ is due to the value of β , which is low enough that passive diffusion of HCO_3^- across the cell membrane is insufficient at higher $\omega = \gamma / q$. (I) The flux to biomass is calculated as $J_B = \min(\gamma C_{in}, \omega H_{in} / q)$. When rubisco activity γ is low, J_B is rubisco-dependent, i.e. depends on γ but not on δ . When γ is larger, however, J_B can be bicarboxylation-limited, i.e. depend on δ (via bicarboxylation) but not on γ . Panel (C) gives $J_{L,tot} / J_B$ as a proxy for the energetic efficiency of growth. Here this value is always negative because $J_{L,tot} < 0$.

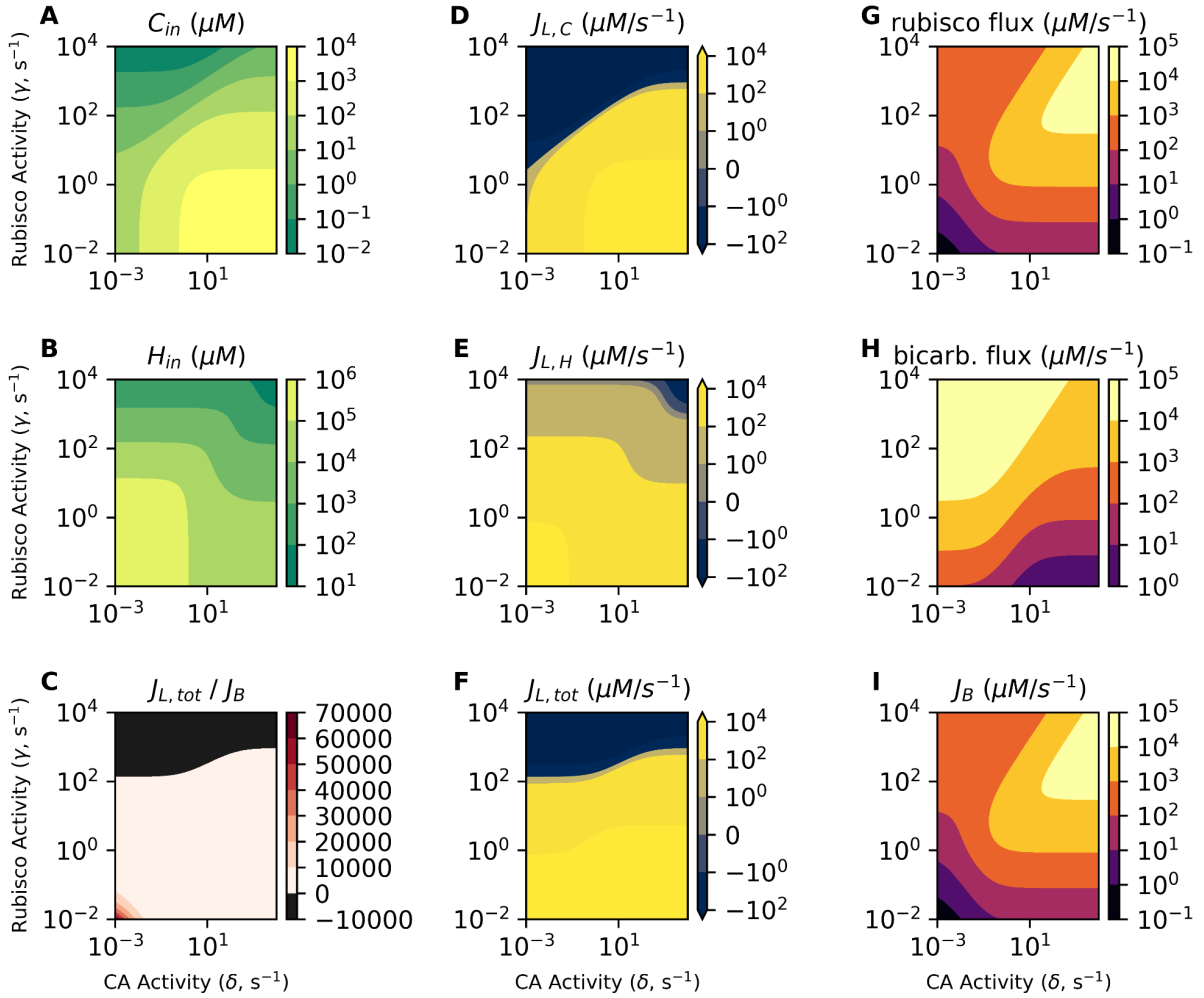


Figure S14: Unrealistically low CO₂ permeabilities permit the co-limitation model to concentrate CO₂ intracellularly. In each panel, the x-axis gives the CA activity δ [s⁻¹] and the y-axis the rubisco activity γ [s⁻¹]. Color in gives the quantity named in each panel title. Here CO₂ permeability $\alpha = 12$ s⁻¹, HCO₃⁻ permeability $\beta = 1.5 \times 10^{-2}$ s⁻¹ and Ci uptake activity $\chi = 100$ s⁻¹ for all panels. (A-B) C_{in} and H_{in} give intracellular CO₂ and HCO₃⁻ concentrations, respectively. Given the low CO₂ permeability α and Ci uptake capacity χ , it is possible for the model to pump CO₂ such that $C_{in} \gg C_{out} = 10$ uM. (D-E) $J_{L,C} = -\alpha(C_{out} - C_{in})$ and $J_{L,H} = -\beta(H_{out} - H_{in})$ represent the flux of CO₂ and HCO₃⁻ leakage from the cell. As we use a large value of χ , both leakage fluxes can adopt large positive values here. (F) $J_{L,tot} = J_{L,C} + J_{L,H}$ is the total flux of Ci leakage from the cell. Notice that $J_{L,H}$ contributes substantially to $J_{L,tot}$ here because of substantial HCO₃⁻ pumping ($\chi \gg 0$). (G) The rubisco carboxylation flux is calculated as γC_{in} and depends strongly on δ because CA activity produces CO₂ from pumped HCO₃⁻ as shown in panel A. Panel (H) gives the bicarboxylation flux ωH_{in} , which also varies with δ and γ . The dependence on γ is an artifact of our assumption that bicarboxylation capacity ω is proportional to γ . The dependence on δ is due to CA-catalyzed conversion of pumped HCO₃⁻ (the bicarboxylation substrate) into CO₂. (I) The flux to biomass is calculated as $J_B = \min(\gamma C_{in}, \omega H_{in} / q)$. In contrast to Figure S13, biomass flux now depends on δ even at low rubisco activities γ . This is due to an unrealistically low value $\alpha = 12$ s⁻¹, which is 1000-fold lower than estimated and measured for biological membranes.

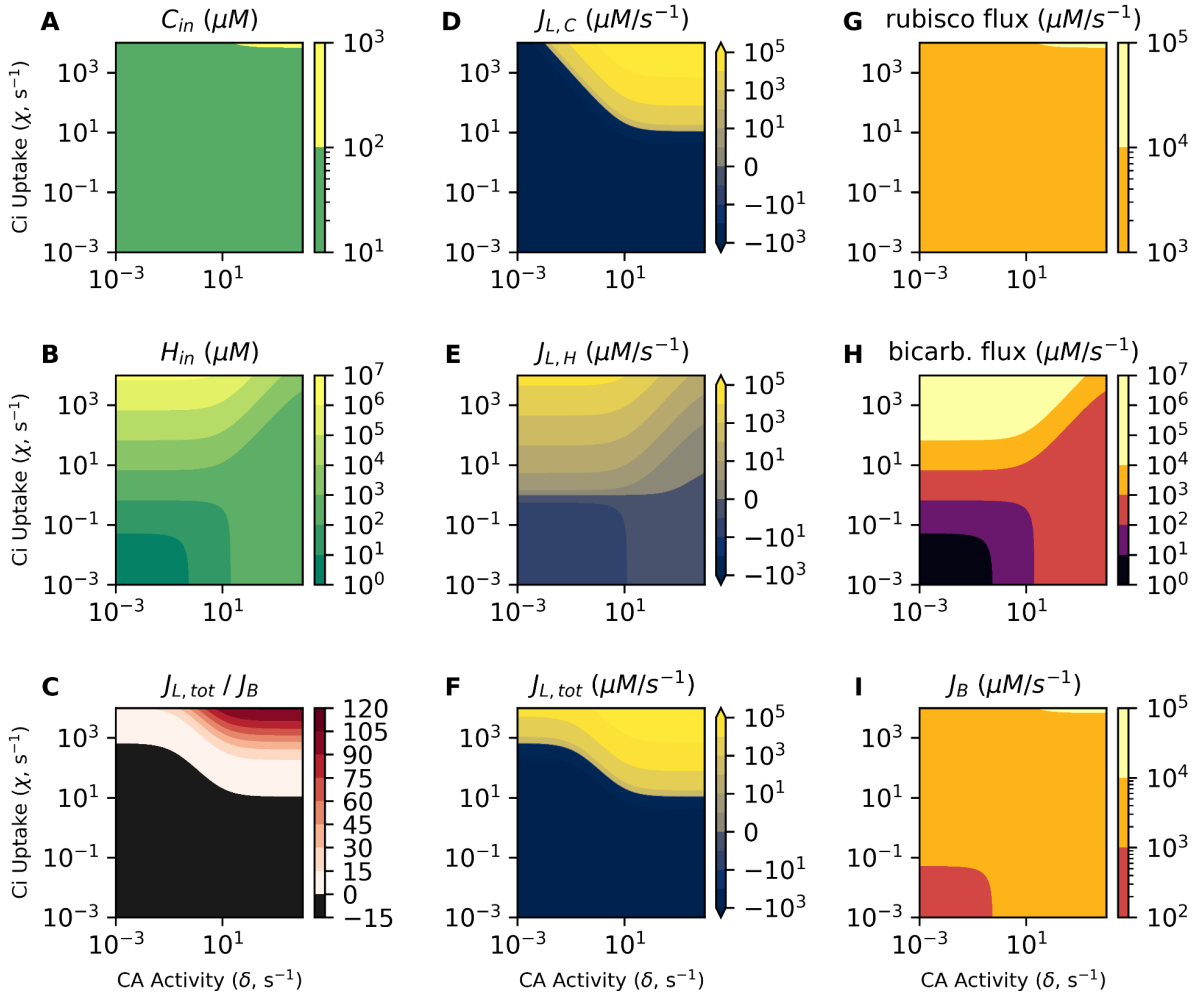


Figure S15: The effects of simultaneously varying CA activity (δ) and Ci uptake (χ) on the co-limitation model of autotrophic growth. In each panel, the x-axis gives the CA activity δ in s^{-1} units and the y-axis the Ci uptake activity χ in the same units. Color in the filled contour plots gives the quantity named in each panel title. The rubisco activity γ was set to $100 s^{-1}$ for all panels. (A-B) C_{in} and H_{in} are the intracellular CO_2 and HCO_3^- concentrations, respectively. (D-E) $J_{L,C} = -\alpha(C_{out} - C_{in})$ and $J_{L,H} = -\beta(H_{out} - H_{in})$ represent the flux of CO_2 and HCO_3^- leakage from the cell. $J_{L,C}$ is positive when $C_{in} > C_{out}$ and negative when $C_{in} < C_{out}$ and there is net passive diffusion of CO_2 into the cell. (F) $J_{L,tot} = J_{L,C} + J_{L,H}$ is the total flux of Ci leakage from the cell. Notice that $J_{L,H}$ only substantially contributes substantially to $J_{L,tot}$ when χ is implausibly high; we calculated a maximum value of $\chi \approx 2 s^{-1}$ from physiological measurements of cyanobacteria, but values of $\chi \approx 10^3 s^{-1}$ are required here for $J_{L,H}$ to contribute noticeably to $J_{L,tot}$ (compare panels D and F). (G) The rubisco carboxylation flux is calculated as γC_{in} . Notice that, consistent with our main-text calculation, there is little variation in C_{in} (panel A) and, therefore, rubisco carboxylation (panel G) across orders of magnitude changes in δ and χ . In contrast, panel (H) gives the bicarboxylation flux ωH_{in} , which varies greatly over the same range due to substantial variation in H_{in} (panel B). (I) The flux to biomass is calculated as $J_B = \min(\gamma C_{in}, \omega H_{in} / q)$. When δ and χ are both low, biomass production is limited by bicarboxylation flux (black region in the lower left) but this limitation is alleviated by increasing either δ or χ . J_B can be increased further if δ and χ are both set to very high values (yellow region on the top right). Panel (C) gives the ratio $J_{L,tot} / J_B$, which is a proxy for the energetic efficiency of autotrophic growth. When $J_{L,tot}$ is large, there is substantial leakage of Ci. This only occurs when χ is large, meaning that energy is “wasted” pumping Ci that subsequently leaks from the cell. $J_{L,tot} \approx 0$ is desirable because it connotes balance between uptake and carboxylation reactions.

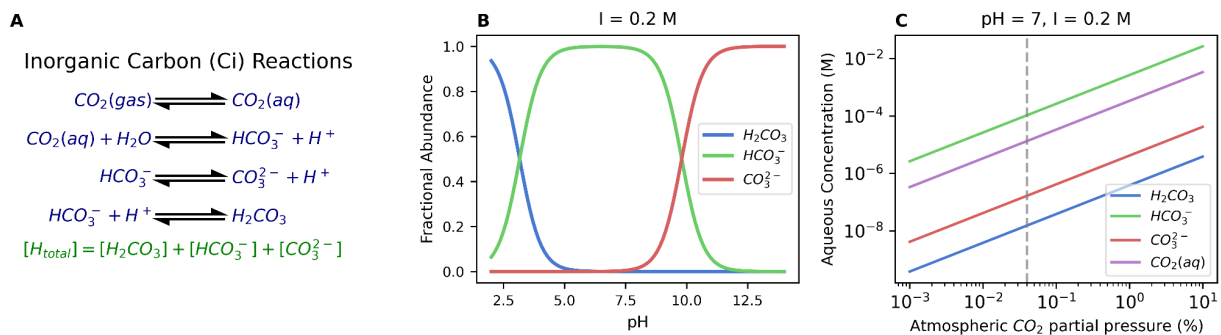


Figure S16: Dependence of inorganic carbon concentrations on pH and atmospheric CO_2 at equilibrium. Panel (A) shows the reactions between inorganic carbon (Ci) species considered here, which are the solubilization of gaseous CO_2 in water, the hydration of aqueous CO_2 to HCO_3^- , and the interconversion of hydrated Ci species - H_2CO_3 , HCO_3^- , and CO_3^{2-} - by protonation and deprotonation reactions. As in (7), we define $[\text{H}_{\text{total}}]$ to be the sum of the hydrated species. Panel (B) gives the speciation of H_{total} as a function of the pH at an ionic strength of 0.2 M, calculated from formation energies reported in (62). (C) gives aqueous concentrations of CO_2 , H_2CO_3 , HCO_3^- , and CO_3^{2-} as a function of the atmospheric CO_2 concentration (pH 7.0 and $I = 0.2 \text{ M}$) assuming that CO_2 is in Henry's law equilibrium with the atmosphere (39).

Supplementary References

1. A. I. Flamholz, *et al.*, Functional reconstitution of a bacterial CO₂ concentrating mechanism in *E. coli*. *Elife* **9** (2020).
2. R. H. Wilson, E. Martin-Avila, C. Conlan, S. M. Whitney, An improved *Escherichia coli* screen for Rubisco identifies a protein-protein interface that can enhance CO₂-fixation kinetics. *J. Biol. Chem.* **293**, 18–27 (2018).
3. B. Xiong, *et al.*, Genome editing of *Ralstonia eutropha* using an electroporation-based CRISPR-Cas9 technique. *Biotechnol. Biofuels* **11**, 172 (2018).
4. B. Kusian, D. Sültemeyer, B. Bowien, Carbonic Anhydrase Is Essential for Growth of *Ralstonia eutropha* at Ambient CO₂ Concentrations. *J. Bacteriol.* **184**, 5018–5026 (2002).
5. C. S. Gai, J. Lu, C. J. Brigham, A. C. Bernardi, A. J. Sinskey, Insights into bacterial CO₂ metabolism revealed by the characterization of four carbonic anhydrases in *Ralstonia eutropha* H16. *AMB Express* **4**, 2 (2014).
6. J. Panich, B. Fong, S. W. Singer, Metabolic Engineering of *Cupriavidus necator* H16 for Sustainable Biofuels from CO₂. *Trends Biotechnol.* (2021).
7. N. M. Mangan, A. Flamholz, R. D. Hood, R. Milo, D. F. Savage, pH determines the energetic efficiency of the cyanobacterial CO₂ concentrating mechanism. *Proc. Natl. Acad. Sci. U. S. A.* **113**, E5354–62 (2016).
8. N. Mangan, M. Brenner, Systems analysis of the CO₂ concentrating mechanism in cyanobacteria. *Elife*, e02043 (2014).
9. A. S. Verkman, Solute and macromolecule diffusion in cellular aqueous compartments. *Trends Biochem. Sci.* **27**, 27–33 (2002).
10. J. T. Mika, B. Poolman, Macromolecule diffusion and confinement in prokaryotic cells. *Curr. Opin. Biotechnol.* **22**, 117–126 (2011).
11. A. I. Flamholz, *et al.*, Revisiting Trade-offs between Rubisco Kinetic Parameters. *Biochemistry* **58**, 3365–3376 (2019).
12. D. Davidi, L. M. Longo, J. Jabłońska, R. Milo, D. S. Tawfik, A Bird's-Eye View of Enzyme Evolution: Chemical, Physicochemical, and Physiological Considerations. *Chem. Rev.* (2018) <https://doi.org/10.1021/acs.chemrev.8b00039>.
13. C. Iñiguez, *et al.*, Evolutionary trends in RuBisCO kinetics and their co-evolution with CO₂ concentrating mechanisms. *Plant J.* **101**, 897–918 (2020).
14. J. Gutknecht, M. A. Bisson, F. C. Tosteson, Diffusion of carbon dioxide through lipid bilayer membranes: effects of carbonic anhydrase, bicarbonate, and unstirred layers. *J. Gen. Physiol.* **69**, 779–794 (1977).
15. T.-X. Xiang, B. D. Anderson, The relationship between permeant size and permeability in lipid bilayer membranes. *J. Membr. Biol.* **140**, 111–122 (1994).

16. C. Hanneschlaeger, A. Horner, P. Pohl, Intrinsic Membrane Permeability to Small Molecules. *Chem. Rev.* **119**, 5922–5953 (2019).
17. V. Endeward, M. Arias-Hidalgo, S. Al-Samir, G. Gros, CO₂ Permeability of Biological Membranes and Role of CO₂ Channels. *Membranes* **7**, 61 (2017).
18. D. H. Turpin, D. B. Layzell, A culture system enabling in situ determination of net and gross photosynthesis, O₂ evolution, N assimilation, and C₂H₂ reduction in cyanobacteria. *Can. J. Bot.* **63**, 1025–1030 (1985).
19. A. Collalti, I. C. Prentice, Is NPP proportional to GPP? Waring's hypothesis 20 years on. *Tree Physiol.* **39**, 1473–1483 (2019).
20. C. Merlin, M. Masters, S. McAteer, A. Coulson, Why is carbonic anhydrase essential to *Escherichia coli*? *J. Bacteriol.* **185**, 6415–6424 (2003).
21. J. Aguilera, J. P. Van Dijken, J. H. De Winde, J. T. Pronk, Carbonic anhydrase (Nce103p): an essential biosynthetic enzyme for growth of *Saccharomyces cerevisiae* at atmospheric carbon dioxide pressure. *Biochem. J.* **391**, 311–316 (2005).
22. P. Burghout, *et al.*, Carbonic anhydrase is essential for *Streptococcus pneumoniae* growth in environmental ambient air. *J. Bacteriol.* **192**, 4054–4062 (2010).
23. K. M. Hines, V. Chaudhari, K. N. Edgeworth, T. G. Owens, M. R. Hanson, Absence of carbonic anhydrase in chloroplasts affects C₃ plant development but not photosynthesis. *Proc. Natl. Acad. Sci. U. S. A.* **118** (2021).
24. E. Magid, B. O. Turbeck, The rates of the spontaneous hydration of CO₂ and the reciprocal reaction in neutral aqueous solutions between 0 degrees and 38 degrees. *Biochim. Biophys. Acta* **165**, 515–524 (1968).
25. R. Milo, R. Phillips, *Cell Biology by the Numbers* (Garland Science, 2015).
26. S.-H. Fan, *et al.*, MpsAB is important for *Staphylococcus aureus* virulence and growth at atmospheric CO₂ levels. *Nat. Commun.* **10**, 3627 (2019).
27. J. Du, B. Förster, L. Rourke, S. M. Howitt, G. D. Price, Characterisation of Cyanobacterial Bicarbonate Transporters in *E. coli* Shows that SbtA Homologs Are Functional in This Heterologous Expression System. *PLoS One* **9**, e115905 (2014).
28. S. Fang, *et al.*, Molecular mechanism underlying transport and allosteric inhibition of bicarbonate transporter SbtA. *Proc. Natl. Acad. Sci. U. S. A.* **118** (2021).
29. J. M. Park, T. Y. Kim, S. Y. Lee, Genome-scale reconstruction and in silico analysis of the *Ralstonia eutropha* H16 for polyhydroxyalkanoate synthesis, lithoautotrophic growth, and 2-methyl citric acid production. *BMC Syst. Biol.* **5**, 101 (2011).
30. H. Knoop, *et al.*, Flux Balance Analysis of Cyanobacterial Metabolism: The Metabolic Network of *Synechocystis* sp. PCC 6803. *PLoS Comput. Biol.* **9** (2013).
31. J. R. Knowles, The Mechanism of Biotin-Dependent Enzymes. *Annu. Rev. Biochem.* **58**, 195–221 (1989).

32. P. V. Attwood, The structure and the mechanism of action of pyruvate carboxylase. *Int. J. Biochem. Cell Biol.* **27**, 231–249 (1995).
33. H. M. Holden, J. B. Thoden, F. M. Raushel, Carbamoyl phosphate synthetase: an amazing biochemical odyssey from substrate to product. *Cell. Mol. Life Sci.* **56**, 507–522 (1999).
34. E. J. Mueller, E. Meyer, J. Rudolph, V. J. Davisson, J. Stubbe, N5-carboxyaminoimidazole ribonucleotide: evidence for a new intermediate and two new enzymatic activities in the de novo purine biosynthetic pathway of *Escherichia coli*. *Biochemistry* **33**, 2269–2278 (1994).
35. I. I. Mathews, T. J. Kappock, J. Stubbe, S. E. Ealick, Crystal structure of *Escherichia coli* PurE, an unusual mutase in the purine biosynthetic pathway. *Structure* **7**, 1395–1406 (1999).
36. J. J. Desmarais, *et al.*, DABs are inorganic carbon pumps found throughout prokaryotic phyla. *Nat Microbiol* **4**, 2204–2215 (2019).
37. M. Shibata, H. Ohkawa, H. Katoh, M. Shimoyama, T. Ogawa, Two CO₂ uptake systems in cyanobacteria: four systems for inorganics carbon acquisition in *Synechocystis* sp. strain PCC 6803. *Funct. Plant Biol.* **29**, 123–129 (2002).
38. G. D. Farquhar, S. von Caemmerer, J. A. Berry, A biochemical model of photosynthetic CO₂ assimilation in leaves of C₃ species. *Planta* **149**, 78–90 (1980).
39. R. Sander, Compilation of Henry's law constants (version 4.0) for water as solvent. *Atmos. Chem. Phys.* **15**, 4399–4981 (2015).
40. I. Schomburg, *et al.*, The BRENDA enzyme information system-From a database to an expert system. *J. Biotechnol.* **261**, 194–206 (2017).
41. Y. M. Bar-On, R. Milo, The global mass and average rate of rubisco. *Proc. Natl. Acad. Sci. U. S. A.* **116**, 4738–4743 (2019).
42. L. Whitehead, B. M. Long, G. D. Price, M. R. Badger, Comparing the in Vivo Function of α -Carboxysomes and β -Carboxysomes in Two Model Cyanobacteria. *Plant Physiol.* **165**, 398–411 (2014).
43. J. L. Collier, S. K. Herbert, D. C. Fork, A. R. Grossman, Changes in the cyanobacterial photosynthetic apparatus during acclimation to macronutrient deprivation. *Photosynth. Res.*, 173–183 (1994).
44. T. Ogawa, A. Kaplan, Inorganic carbon acquisition systems in cyanobacteria. *Photosynth. Res.* **77**, 105–115 (2003).
45. B. D. Rae, B. M. Long, M. R. Badger, G. D. Price, Functions, compositions, and evolution of the two types of carboxysomes: polyhedral microcompartments that facilitate CO₂ fixation in cyanobacteria and some proteobacteria. *Microbiol. Mol. Biol. Rev.* **77**, 357–379 (2013).
46. G. D. Price, M. R. Badger, Expression of Human Carbonic Anhydrase in the Cyanobacterium *Synechococcus* PCC7942 Creates a High CO₂-Requiring Phenotype Evidence for a Central Role for Carboxysomes in the CO₂ Concentrating Mechanism. *Plant Physiol.* **91**, 505–513 (1989).

47. A. Flamholz, P. M. Shih, Cell biology of photosynthesis over geologic time. *Curr. Biol.* **30**, R490–R494 (2020).
48. J. A. Bassham, Mapping the carbon reduction cycle: a personal retrospective. *Photosynth. Res.* **76**, 35–52 (2003).
49. A. Bar-Even, A. Flamholz, E. Noor, R. Milo, Thermodynamic constraints shape the structure of carbon fixation pathways. *Biochim. Biophys. Acta* **1817**, 1646–1659 (2012).
50. G. C. Cannon, S. Heinhorst, C. a. Kerfeld, Carboxysomal carbonic anhydrases: Structure and role in microbial CO₂ fixation. *Biochim. Biophys. Acta* **1804**, 382–392 (2010).
51. L. M. Oltrogge, *et al.*, Multivalent interactions between CsoS2 and Rubisco mediate α -carboxysome formation. *Nat. Struct. Mol. Biol.* **27**, 281–287 (2020).
52. S. H. Baker, S. Jin, H. C. Aldrich, G. T. Howard, J. M. Shively, Insertion mutation of the form I *cbbL* gene encoding ribulose biphosphate carboxylase/oxygenase (RuBisCO) in *Thiobacillus neapolitanus* results in expression of form II RuBisCO, loss of carboxysomes, and an increased CO₂ requirement for growth. *J. Bacteriol.* **180**, 4133–4139 (1998).
53. Y. Sun, *et al.*, Decoding the Absolute Stoichiometric Composition and Structural Plasticity of α -Carboxysomes. *MBio*, e0362921 (2022).
54. J. N. Kinney, S. D. Axen, C. a. Kerfeld, Comparative analysis of carboxysome shell proteins. *Photosynth. Res.* **109**, 21–32 (2011).
55. C. A. Hutchison 3rd, *et al.*, Polar Effects of Transposon Insertion into a Minimal Bacterial Genome. *J. Bacteriol.* **201** (2019).
56. K. M. Scott, *et al.*, Diversity in CO₂-Concentrating Mechanisms among Chemolithoautotrophs from the Genera *Hydrogenovibrio*, *Thiomicrothrix*, and *Thiomicrospira*, Ubiquitous in Sulfidic Habitats Worldwide. *Appl. Environ. Microbiol.* **85**, 1–19 (2019).
57. N. M. Wheatley, C. D. Sundberg, S. D. Gidaniyan, D. Cascio, T. O. Yeates, Structure and identification of a pterin dehydratase-like protein as a ribulose-bisphosphate carboxylase/oxygenase (RuBisCO) assembly factor in the α -carboxysome. *J. Biol. Chem.* **289**, 7973–7981 (2014).
58. K. A. Johnson, R. S. Goody, The Original Michaelis Constant: Translation of the 1913 Michaelis–Menten Paper. *Biochemistry* (2011).
59. Gunawardena J, J. Gunawardena, D. Kellogg, Some lessons about models from Michaelis and Menten. *Mol. Biol. Cell* **23**, 517–519 (2012).
60. D. Davidi, *et al.*, Highly active rubiscos discovered by systematic interrogation of natural sequence diversity. *EMBO J.*, e104081 (2020).
61. D. Liu, R. C. S. Ramya, O. Mueller-Cajar, Surveying the expanding prokaryotic Rubisco multiverse. *FEMS Microbiol. Lett.* **364** (2017).
62. R. A. Alberty, *Thermodynamics of Biochemical Reactions*, 1st Ed. (John Wiley & Sons, 2003).

